

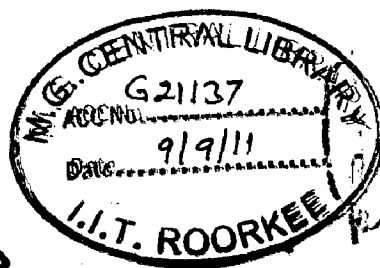
MODELING AND SIMULATION OF NANOWIRE SOLAR CELLS

A DISSERTATION

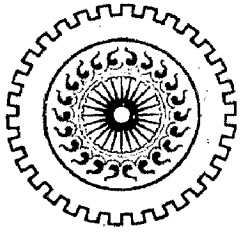
Submitted in partial fulfillment of the requirements for the award of the degree of
MASTER OF TECHNOLOGY
in
NANOTECHNOLOGY

By

JITENDRA KUMAR



**CENTRE OF NANOTECHNOLOGY
INDIAN INSTITUTE OF TECHNOLOGY ROORKEE
ROORKEE-247 667 (INDIA)
JUNE, 2011**



Indian Institute of Technology Roorkee


Centre of Nanotechnology

Candidate Declaration

I hereby declare that the work, which is being presented in this Dissertation entitled “**MODELING AND SIMULATION OF NANOWIRE SOLAR CELLS**” submitted in partial fulfillment of the requirement for the award of degree of **Master of Technology** with specialization in **Nanotechnology**, submitted in the **Centre of Nanotechnology, Indian Institute of Technology Roorkee**, is an authentic record of my own work carried out from July 2010 to June 2011, under the guidance of **Dr. Sanjeev Manhas** and **Dr. Dharmendra Singh**, Department of Electronics and Communication Engineering, Indian Institute of Technology, Roorkee.

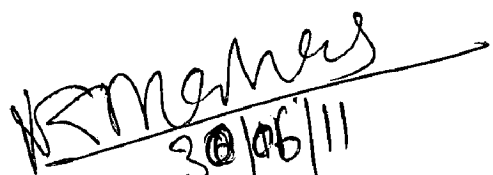
The matter embodied in this dissertation has not been submitted for the award of any other degree.


Date: 30/06/11


(Jitendra Kumar)

Place: Roorkee

This is to certify that the above statement made by the candidate is correct to the best of my knowledge.


(Dr. SANJEEV MANHAS)
Assistant Professor
E&C Department
Indian Institute of Technology Roorkee


(Dr. DHARMENDRA SINGH)
Associate Professor
E&C Department
Indian Institute of Technology Roorkee

Acknowledgements

First and foremost, I would like to express my sincere gratitude towards my parents for giving me this beautiful gift of education. Truly without their blessing, motivation and inspiration I could not have achieve this much.

I wish to record my deep appreciation to my supervisors Dr. Sanjeev Manhas and Dr. Dharmendra Singh for their invaluable guidance and advice as to which path to pursue in my Dissertation work. I also sincerely appreciated the help rendered by them and their professional attitude whenever I met obstacles during my research work.

I would like to thank Satish (Research Scholar), who have helped me to solve the endless problems that I have encountered in Synopsys-TCAD software during the course of my Dissertation work.

Personally, I would like to thank chotu, Motu, Satya, Linux, Swati for being my best friends in the past few years and helping me get through the tough days. I am grateful for their support and encouragement. When I saw black clouds ahead and failures, these people always showed me a silver lining and reasons to keep trying.

Thank to all my friends for making it fun.

Jitendra Kumar

June 2011

Roorkee, India

Contents

Candidate Declaration	i
Acknowledgements	ii
Abstract	iii
Contents	iv
List of Figures	vii
List of Tables	ix
1 Solar Cell Device Physics	1
1.1 Introduction	1
1.2 Solar Illumination	3
1.3 Solar Cell Characterization Parameters	4
(a) Short Circuit Current	5
(b) Open Circuit Voltage	5
(c) Maximum Power	5
(d) Fill Factor	6
(e) External Quantum Efficiency	6
(f) Conversion Efficiency	6
1.4 Recombination Losses	6
1.4.1 Shockley Read Hall Recombination	7
1.4.2 Band to Band Recombination	7
1.4.3 Auger Recombination	7
1.4.4 Surface Recombination	8
1.5 Multijunction Solar Cells Concept	8
2 Literature Review	11
2.1 Current Photovoltaic Technology	11
2.2 Current Limitations of Planar Junction Solar Cells	12
2.3 Advantages of Nanowire Based Solar Cells	13
2.3.1 Defect Density Tolerance	13
2.2.2 Light Scattering Effect	14
2.2.3 Light Trapping Effect	14
2.2.4 High Surface Area	15

Acknowledgements

First and foremost, I would like to express my sincere gratitude towards my parents for giving me this beautiful gift of education. Truly without their blessing, motivation and inspiration I could not have achieved this much.

I wish to record my deep appreciation to my supervisors Dr. Sanjeev Manhas and Dr. Dharmendra Singh for their invaluable guidance and advice as to which path to pursue in my Dissertation work. I also sincerely appreciated the help rendered by them and their professional attitude whenever I met obstacles during my research work.

I would like to thank Satish (Research Scholar), who have helped me to solve the endless problems that I have encountered in Synopsys-TCAD software during the course of my Dissertation work.

Personally, I would like to thank chotu, Motu, Satya, Linux, Swati for being my best friends in the past few years and helping me get through the tough days. I am grateful for their support and encouragement. When I saw black clouds ahead and failures, these people always showed me a silver lining and reasons to keep trying. Thank to all my friends for making it fun.

Jitendra Kumar

June 2011

Roorkee, India

Abstract

Recently nanomaterials like Nanowire (NW), nanoparticle and quantum dot have shown to have important characteristics like larger surface to volume ratio and quantum confinement effects that can be exploited by using them as an active element in the solar cells. NW structured solar cells have shown promising potential for integrated power source for nanoelectronics systems such as driving element for nanowire sensors and logic gates.

In this thesis, we report 3D-TCAD study of lateral p-type/intrinsic/n-type (p-i-n) coaxial, vertical pn and multijunction NW solar cells. We have modeled electric field inside the radial and planar structures showing advantages of radial structures. The performance of NW solar cell is benchmarked with similar dimension planar structure under same illumination conditions. The doping densities of p-core, n-shell and thickness of intrinsic shell are optimized. The effect of using low quality material on solar cell performance is also investigated. The studies shows that for a given level of defect density radial structure gives overall higher efficiency than planar structure. Our results have significant importance for design of vertical NW based solar cells and applications.

We also investigated a novel NW based multijunction solar cell. This structure utilizes concept of splitting incoming energy spectrum into multiple (two for our structure) segments, each of which contribute to charge generation separately to enable more efficient charge collection. The result show enhanced efficiency of up to 20%.

Contents

Candidate Declaration	i
Acknowledgements	ii
Abstract	iii
Contents	iv
List of Figures	vii
List of Tables	ix
1 Solar Cell Device Physics	1
1.1 Introduction	1
1.2 Solar Illumination	3
1.3 Solar Cell Characterization Parameters	4
(a) Short Circuit Current	5
(b) Open Circuit Voltage	5
(c) Maximum Power	5
(d) Fill Factor	6
(e) External Quantum Efficiency	6
(f) Conversion Efficiency	6
1.4 Recombination Losses	6
1.4.1 Shockley Read Hall Recombination	7
1.4.2 Band to Band Recombination	7
1.4.3 Auger Recombination	7
1.4.4 Surface Recombination	8
1.5 Multijunction Solar Cells Concept	8
2 Literature Review	11
2.1 Current Photovoltaic Technology	11
2.2 Current Limitations of Planar Junction Solar Cells	12
2.3 Advantages of Nanowire Based Solar Cells	13
2.3.1 Defect Density Tolerance	13
2.2.2 Light Scattering Effect	14
2.2.3 Light Trapping Effect	14
2.2.4 High Surface Area	15

2.2.5	Wider Range of Materials/Heterostructures	15
2.2.6	High Built-in Electric Field	15
3	Simulation Tools and Methodology	17
3.1	Introduction to Device Simulation	17
3.2	Sentaurus Structure Editor	17
3.3	Sentaurus Device	18
(a)	File Section	18
(b)	Electrode Section	19
(c)	Physics Section	19
(d)	Plot Section	19
(e)	Math Section	19
(f)	Solve Section	19
3.4	Tecplot SV	20
3.5	Inspect	20
4	Built-in Electric Field Modeling	21
4.1	Electric Field Modeling inside PIN-NW Structure	21
4.2	Electric Field Modeling inside PIN-Planar Structure	24
4.3	Modeled and Simulated Electric Field Comparison in Radial and Planar PIN-Structures	25
4.4	Electric Field Modeling inside PN-Nanowire Structure	26
4.5	Electric Field Modeling inside PN-Planar Structure	27
4.6	Modeled and Simulated Electric Field Comparison in Radial and Planar PN-Structures	28
4.7	Summary	28
5	Lateral PIN-Nanowire Solar Cell	29
5.1	Structure Details	29
5.2	Structural Parameters Optimization	30
5.3	Illumination Angle Study	34
5.4	Summary	36

6	Vertical PN-Nanowire Single and Multijunction Solar Cell	37
6.1	Vertical PN-Nanowire Solar Cell	37
6.1.1	Structure Details	37
6.1.2	Structural Parameters Optimization	38
6.1.3	Summary	41
6.2	Multijunction Solar Cell	42
6.2.1	Structure Details	42
6.2.2	Results and Discussion	43
6.2.3	Summary	45
7	Conclusion and Future Work	47
	Bibliography	49
	Publications	52

List of Figures

1.1	Schematic of air mass	3
1.2	Schematic of simple single junction planar solar cell	4
1.3	Schematic of solar cell IV characteristics	5
1.4	Schematic of different kind of recombination in a typical solar cell	8
1.5	On left, a schematic of photon absorption in GaAs Solar cell; on right solar spectrum (in black) and power converted by GaAs solar cell (shaded area)	9
1.6	On left, a schematic of photons that are absorbed in four junction solar cell; on right, a solar spectrum (in black) and power converted by each of four sub cells (shaded regions)	10
2.1	Schematic of conventional planar junction solar cell	12
2.2	Schematic of NW based pn junction solar cell	13
2.3	Schematic of NW array solar cell with light scattering effect	14
2.4	Schematics of coaxial NW with light trapping effect	15
3.1	A typical sentaurus structure editor	18
3.2	Schematic of input and output file flow in sentaurus device	19
3.3	A typical tecplot of sentaurus device	20
4.1	Cross section of cylindrical junction PIN diode	21
4.2	Cross section of planar junction PIN diode	24
4.3	Modeled and simulated E-field (a) radial structure, (b) planar structure	25
4.4	Cross section of radial junction PN diode	26
4.5	Cross section of planar junction PN diode	27
4.6	Modeled and simulated E-field (a) radial structure, (b) planar structure	28
5.1	Structure of the co-axial NW PIN-junction solar cell	29
5.2	Structure of the planar PIN-junction solar cell	29
5.3	Characteristics of radial and planar structures for different amount of doping in n-layer (a) I_{sc} , (b) V_{oc} and (c) conversion efficiency	31
5.4	Characteristics of radial and planar structure for different amount of doping in p-layer (a) I_{sc} , (b) V_{oc} and (c) conversion efficiency	32
5.5	Characteristics of radial and planar structure for different thickness of i-layer (a) I_{sc} , (b) V_{oc} and (c) conversion efficiency	33

5.6	Characteristics of radial and planar structure for different amount defect density (a) I_{sc} , (b) V_{oc} and (c) conversion efficiency	34
5.7	Characteristics of structures with and without oxide layer for different angle of illuminations (a) I_{sc} (b) V_{oc} and (c) conversion efficiency	35
5.8	EQE for structure with SiO_2 layer at different angle of incident	36
6.1	On left, 3D view of vertical co-axial PN-junction NW solar cell structure used in this simulation study; on left, 2D cross section view of the same structure	37
6.2	On left, 3D view of PN-planar junction solar cell structure used for bench marking, in this simulation study; on left, 2D cross section view of the same structure	38
6.3	Characteristics of radial and planar structures for different amount of doping in n-layer (a) I_{sc} , (b) V_{oc} and (c) conversion efficiency	39
6.5	Characteristics of radial and planar structure for different amount of doping in p-layer (a) I_{sc} , (b) V_{oc} and (c) conversion efficiency	40
6.6	Characteristics of radial and planar structure for different amount defect density (a) I_{sc} , (b) V_{oc} and (c) conversion efficiency	41
6.7	Structure of multijunction solar cell	42
6.8	Characteristics of GaAs NW cell for different n-shell doping (a) I_{sc} , (b) V_{oc} and (c) conversion efficiency	43
6.9	Characteristics of GaAs NW cell for different p-core doping (a) I_{sc} , (b) V_{oc} and (c) conversion efficiency	43
6.10	Band diagrams of tunnel diode for different doping density	44

List of Tables

5.1	Structure parameters of un-optimized lateral NW solar cell	30
6.1	Structure parameters of un-optimized vertical NW solar cell	38
6.2	Structure parameters of un-optimized NW multijunction solar cell	43

Chapter 1

Solar Cell Device Physics

1.1 Introduction

Supply of energy is one of the main concerns of our society. Because of our growing economy and modern lifestyle, consumption of energy rises drastically. On the other hand, the primary energy sources, i.e. the fossil energy sources, have limited reserves-oil for about 40 years, gas for about 70 years, and coal for about 200 years only [1]. The current oil prize instability reveals the vulnerability of our economy towards higher energy prices, not mentioning the political and economical unrest predominant in several main oil producing countries. Because our Country is highly depends on these supplies, there is a risk of slipping into an energy crisis someday soon.

Another major reason for the necessity of a change towards regenerative energy sources is found in the global warming caused by air pollution on account of the carbon dioxide emission using fossil fuels. One alternative would be to substitute fossil energy by nuclear power, but the disposal and handling of the radioactive material is a problematic and involves much danger, unsolved issue until now. One of the most viable ways to solve the foreseeable world's energy crisis is to utilize the power of the sun. The energy we are getting from the sun is huge; actually 1 hour of solar radiation on earth is equivalent to the total world energy consumption in 1 year [2]. To utilize this energy direct conversion of solar radiation into electricity by solar cells has been examined and developed for several decades.

Silicon is most popular material choice for terrestrial solar cells. This is for several reasons. Firstly, silicon's bandgap almost ideally match to the solar spectrum [3]. Secondly, silicon is most abundant and cheap material on earth [4]. Thirdly, by using silicon, photovoltaic industry can utilize the wealth of knowledge that microelectronics industry has acquired over several decades of experience. Nowadays, about 85% of the worldwide solar cell production is based on silicon [5]. However, the market for photovoltaic applications being one of the fastest growing at present time, In order to reach this goal, scientific teams in companies and academia are investigating ways to

improve the efficiency of the cells and at the same time also trying to reduce the cost of solar cell.

At present, material and production costs of the existing inorganic semiconductor-based (i.e. silicon based) technology are still too high for a widespread substitution of fossil energy by energy production through solar cell. Therefore, a widespread attention is currently focused on new types of solar cell structure and materials, such as thin film, polymer, dye sensitized and NW based solar cell. Among them, NW based solar cells are seriously considered as potential candidates for the next generation of solar cells. Although till now the efficiency of such solar cells cell could not stand yet in comparison with the ones obtained with planar junction semiconductor solar cells [6-7], but cost factor should be kept in mind. NW based solar cells could potentially be produced in a much more cost effective way. The price for the material is quite low, and the production steps are very simple and considerably cheaper than planer semiconductor solar cells.

NW structured solar cells have shown promising potential for integrated power source for nanoelectronics systems such as driving element for nanowire sensors, logic gates [9] etc. The nanoparticles/nanowires have been used to improve the charge collection efficiency in polymer blend [7] and dye sensitized [8] solar cells. Further recent theoretical studies have indicated that solar cell having junction in radial direction has better solar cell performance characteristics than its planar counterpart [9]. This is because of orthogonalization of light and charge carrier transport. Which means that even with the low quality material radial junction based solar cell gives higher conversion efficiency than planar counterpart. Similarly Bozhi Tian et al. has physically fabricated lateral PIN-NW solar cell in self powered circuits and reported the efficiency of around 3.4 percent [9].

Different groups [11-12] have also fabricated vertical NW solar cell using bottom up approach but the conversion efficiency reported in these studies is quite low. In a recent study by W.F. Liu et al. reported strong enhancement of light absorption in single lateral silicon coaxial NW core (silicon)/shell (dielectric) type structure [13]. This enhancement of light trapping provides another dimension for designing of lateral NW based solar cell.

Professionals in the solar cell community have been trying to reduce the cost of the solar cell by using some innovative ideas to fabricate NW solar cells like [14-15] has

used VLS method to grow NW solar cells and [16] has grown NW solar cells using silica beads synthesis. But very few studies have been done on studying the parameters that affect and guide the performance of solar cells. For full utilization of solar cell potential we need to understand and optimize the parameters that affect and guide its performance.

1.2 Solar Illumination

When solar radiation travel through the atmosphere, it gets attenuates, which is mainly due to water-vapour absorption in the infrared, ozone absorption in the ultraviolet, and scattering by airborne dust [17]. The degree to which atmosphere affects the solar radiation received at the earth's surface is defined by the "Air Mass". Air mass is defined as the secant of the angle between the sun and the zenith (Θ) and measures the atmospheric path length relative to the minimum path length when the sun is directly overhead.

$$AM = \frac{1}{\cos \theta} \quad (1.1)$$

Air Mass is followed by a number, which refers to the length of the path through the atmosphere in relation to the shortest length if the sun was in the apex [18].

Here in our simulation study, we have used A.M. 1.5G solar spectrum." Air Mass 1.5" indicates that the solar light has been attenuated by passage through the Earth's atmosphere a distance equal to 1.5 times the shortest path (which is when the sun is directly over head). "Global" indicates that both direct and diffuse components of solar radiation are included.

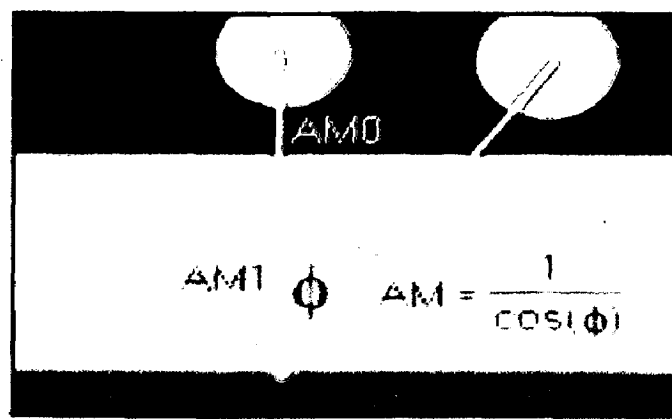


Figure 1.1 Schematic of air mass [19].

(d) *Fill Factor (FF)*: The Fill Factor (FF) is essentially a measure of quality of the solar cell. It is calculated by comparing the maximum power (P_{max}) to theoretical power (P_T) and is given as [17-18].

$$FF = \frac{P_{max}}{P_T} \quad (1.8)$$

$$= \frac{V_{max} \cdot I_{max}}{V_{oc} \cdot I_{sc}} \quad (1.9)$$

(e) *External Quantum Efficiency*: External quantum efficiency (EQE) is the number of carrier collected to produce the photocurrent divided by number of incident photons.

$$\eta_{ext} = (I_l/q)/(P_{opt}/hv) \quad (1.10)$$

where I_l is the photogenerated current by the absorption of incident optical power P_{opt} , at a wavelength λ (corresponding to a photon energy hv).

(f) *Conversion Efficiency*: It is the ratio of the electrical power output P_{out} to the solar power input, P_{in} , into the solar cell [17-18].

$$\eta = \frac{P_{out}}{P_{in}} \quad (1.11)$$

$$= \frac{V_{oc} \cdot I_{sc} \cdot FF}{P_{in}} \quad (1.12)$$

In our work input power is calculated by multiplying power density of solar spectrum ($0.1W/cm^2$) with area of solar cell on which solar illumination incident. For lateral NW structure this area is calculated by multiplying NW length excluding contact length with the diameter of NW. For vertical NW structure this area is the top cross section area of the solar cell. For multijunction solar cell this area is the cross section area of bottom solar cell.

1.4 Recombination Losses

The performance of solar cell is limited by the recombination process that occurs in the solar cell, which basically reduces the effective collection of charge carrier.

There are following recombination processes that limit the charge collection efficiency of a solar cell.

1.4.1 Shockley Read Hall Recombination

It is the dominant form of recombination mechanism in most of the solar cells. In this type of recombination due to the impurities present in the semiconductor an additional energy level is introduced within the forbidden energy gap. This energy level acts as a trap and captures electrons and holes, leading to recombination.

The relationship between recombination rate (U) (in unit of cm^{-3}/s) and trap density (N_t) (in unit of cm^{-3}) is given by relation [17].

$$U = \frac{\sigma_p \sigma_n v_{th} (pn - n_i^2) N_t}{\sigma_n \left[n + n_i \exp\left(\frac{E_t - E_i}{kT}\right) \right] + \sigma_p \left[p + n_i \exp\left(\frac{-(E_t - E_i)}{kT}\right) \right]} \quad (1.13)$$

Where,

σ_p = hole capture cross-section, n_i = intrinsic carrier density, v_{th} = thermal velocity
 σ_n = electron capture cross-section, E_i = intrinsic energy level, N_t = trap density

1.4.2 Band to Band Recombination

It is a radiative form of recombination in which an electron from conduction band recombines with the hole in the valence band with emission of energy [18]. Band to band recombination mainly occurs in direct band gap semiconductors. The probability of occurrence of this form of recombination in indirect band gap semiconductor is very low.

1.4.3 Auger Recombination

This type of recombination occurs in heavily doped semiconductors. In this recombination mechanism hole from the valence band recombines with the electron in the conduction band. The excess energy released during this recombination is absorbed by the neighboring electron in the conduction band, which then goes to some higher energy level and then again falls back to the conduction band with release of energy [18].

The Figure 1.4 shows all three kinds of recombination discussed above.

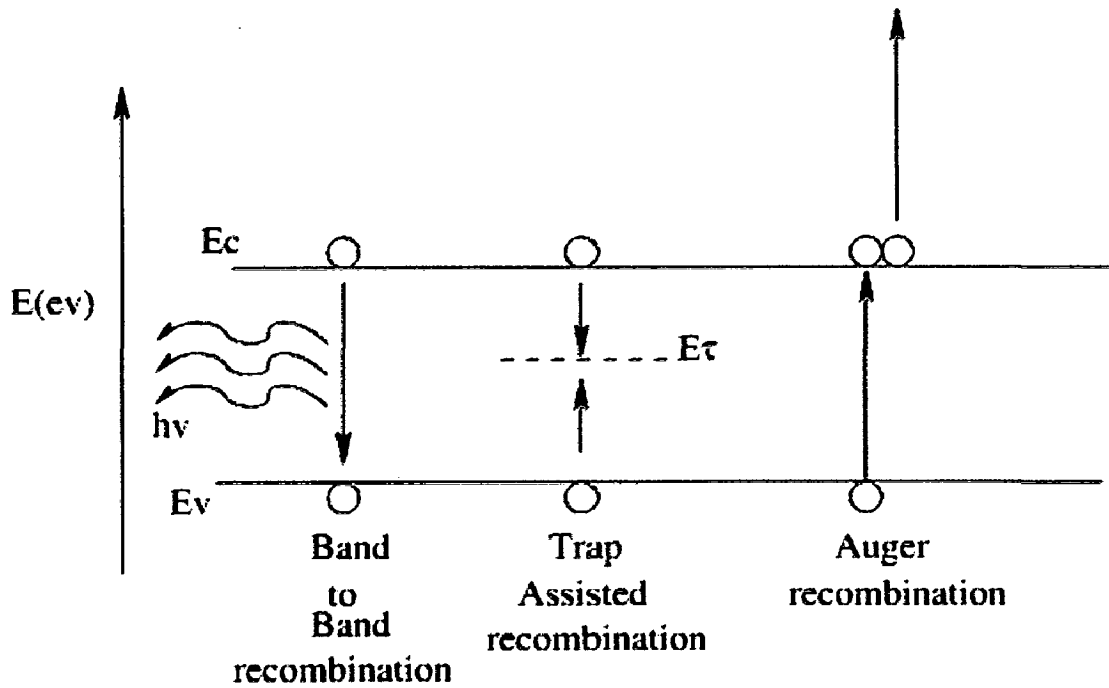


Figure 1.4 Schematic of different kind of recombination in a typical solar cell [18].

1.4.4 Surface Recombination

Because of abrupt termination of crystal structure, semiconductor surface has large number of dangling bonds. These dangling bond acts as recombination centers for charge carriers. Carriers generated near the surface fall in to these dangling bonds and gets recombine.

1.5 Multijunction Solar Cells Concept

With a traditional single junction solar cell, much of the incident light energy is not converted into electricity. If an incident photon has less energy than the semiconductor bandgap, the photon cannot be absorbed since there is not enough energy to excite an electron from the conduction band to the valence band. Therefore, none of the light with less energy than the semiconductor bandgap is used in the solar cell. If an incident photon has more energy than the bandgap, the excess energy will be lost in the form of heat.

Figure 1.5 shows the schematic of the photons that are absorbed in GaAs solar cell; on right, a plot showing the solar spectrum (in black) and the power converted by the GaAs cell (shaded green area). The maximum theoretical efficiency of this solar cell is 30% [20].

used VLS method to grow NW solar cells and [16] has grown NW solar cells using silica beads synthesis. But very few studies have been done on studying the parameters that affect and guide the performance of solar cells. For full utilization of solar cell potential we need to understand and optimize the parameters that affect and guide its performance.

1.2 Solar Illumination

When solar radiation travel through the atmosphere, it gets attenuates, which is mainly due to water-vapour absorption in the infrared, ozone absorption in the ultraviolet, and scattering by airborne dust [17]. The degree to which atmosphere affects the solar radiation received at the earth's surface is defined by the "Air Mass". Air mass is defined as the secant of the angle between the sun and the zenith ($\sec \theta$) and measures the atmospheric path length relative to the minimum path length when the sun is directly overhead.

$$AM = \frac{1}{\cos \theta} \quad (1.1)$$

Air Mass is followed by a number, which refers to the length of the path through the atmosphere in relation to the shortest length if the sun was in the apex [18].

Here in our simulation study, we have used A.M. 1.5G solar spectrum. "Air Mass 1.5" indicates that the solar light has been attenuated by passage through the Earth's atmosphere a distance equal to 1.5 times the shortest path (which is when the sun is directly over head). "Global" indicates that both direct and diffuse components of solar radiation are included.

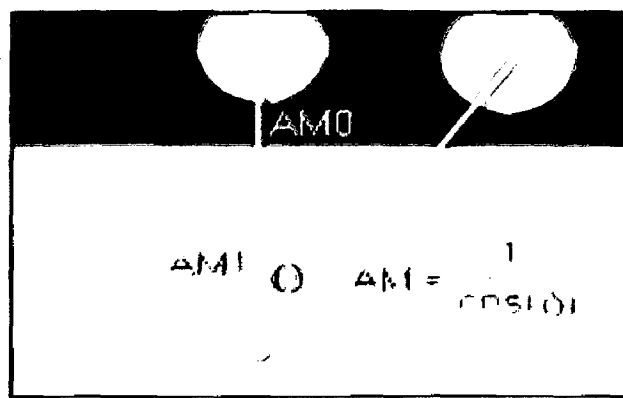


Figure 1.1 Schematic of air mass [19].

1.3 Solar Cell Characterization Parameters

Solar cell converts energy, which is in the form of photons into electricity via an excited state. In solar cells made of semiconductor materials, each absorbed photon excites an electron from the valance band to the conduction band, producing an electron-hole pair. These carriers diffuse through the quasi-neutral material until they reach the pn-junction where drift caused by the built-in electric field separates the carriers. For example, in Figure 1.2 holes move to the bottom of the cell while electrons move to the top the cell. This process produces a current which can be extracted.

A solar cell often consist of the semiconductor pn-junction with a solid back metal contact, metal fingers on the top surfaces as a top contact, and an anti-reflective coating on the top surface [20].

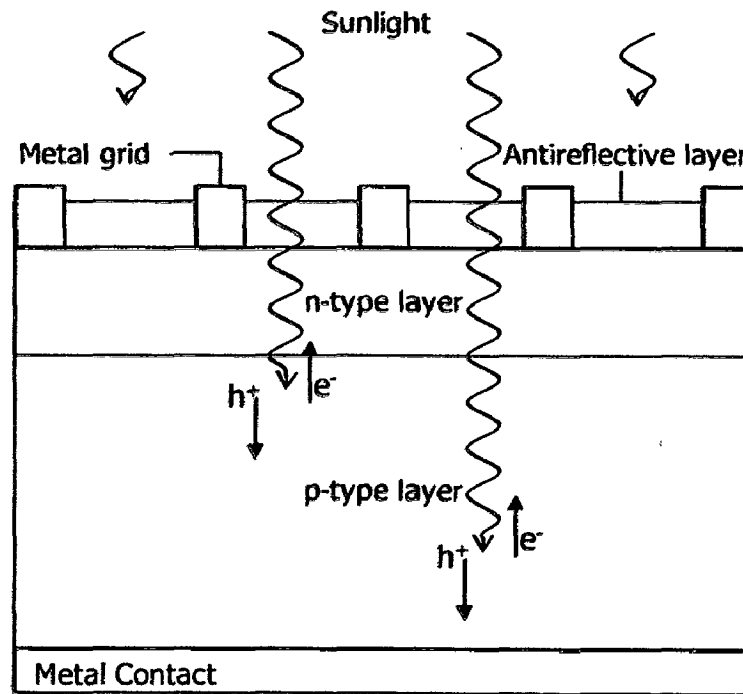


Figure 1.2 Schematic of simple single junction planar solar cell.

The current–voltage curve provides the basics for the characterization of solar cell performance. In an ideal cell, the total current I is equal to the current I_l (photo current) minus the diode current I_D [17-18].

$$I = I_l - I_D \quad (1.2)$$

$$= I_l - I_o (e^{qV/kT} - 1) \quad (1.3)$$

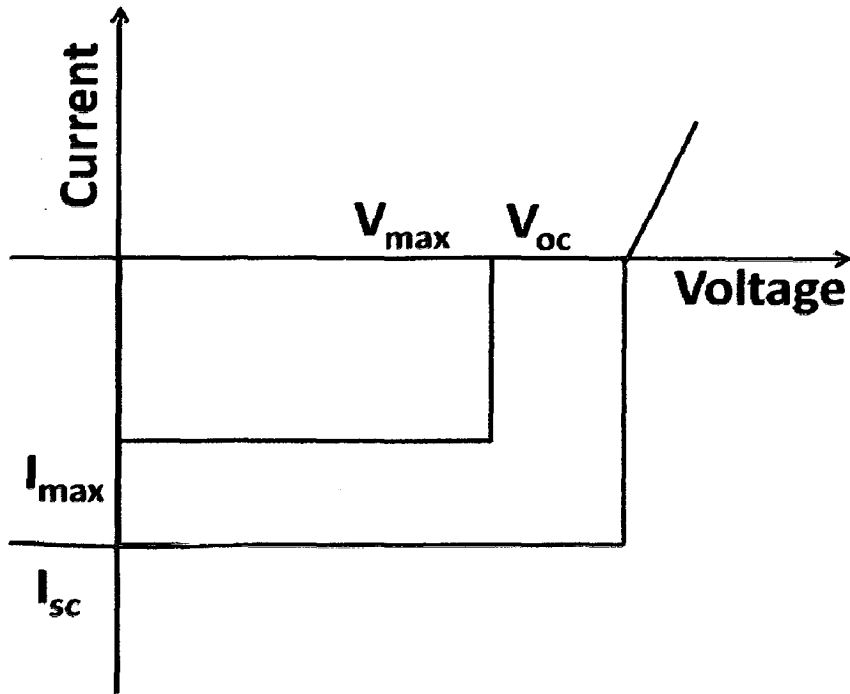


Figure 1.3 Schematic of solar cell IV characteristics.

(a) *Short Circuit Current (I_{sc})*: It is the current that flows through the solar cell, when no external voltage is applied.

$$I(\text{at } V = 0) = I_{sc} \quad (1.4)$$

(b) *Open Circuit Voltage (V_{oc})*: It is the voltage when no current is flowing through it i.e. under open circuit condition.

$$V(\text{at } I = 0) = V_{oc} \quad (1.5)$$

The open circuit voltage and short circuit current is related to each other via following relationship

$$V_{oc} = \frac{kT}{q} \ln \left(\frac{I_{sc}}{I_o} + 1 \right) \quad (1.6)$$

Where,

I_o = recombination current
 q = charge

k = Boltzmann constant
 T = Temperature in Kelvin

(c) *Maximum Power (P_{max})*: It is the maximum power that is available at the output of the solar cell. It is given as the product maximum voltage and maximum current.

$$P_{max} = V_{max} \cdot I_{max} \quad (1.7)$$

(d) *Fill Factor (FF)*: The Fill Factor (FF) is essentially a measure of quality of the solar cell. It is calculated by comparing the maximum power (P_{max}) to theoretical power (P_T) and is given as [17-18].

$$FF = \frac{P_{max}}{P_T} \quad (1.8)$$

$$= \frac{V_{max} \cdot I_{max}}{V_{oc} \cdot I_{sc}} \quad (1.9)$$

(e) *External Quantum Efficiency*: External quantum efficiency (EQE) is the number of carrier collected to produce the photocurrent divided by number of incident photons.

$$\eta_{ext} = (I_l/q)/(P_{opt}/hv) \quad (1.10)$$

where I_l is the photogenerated current by the absorption of incident optical power P_{opt} , at a wavelength λ (corresponding to a photon energy hv).

(f) *Conversion Efficiency*: It is the ratio of the electrical power output P_{out} to the solar power input, P_{in} , into the solar cell [17-18].

$$\eta = \frac{P_{out}}{P_{in}} \quad (1.11)$$

$$= \frac{V_{oc} \cdot I_{sc} \cdot FF}{P_{in}} \quad (1.12)$$

In our work input power is calculated by multiplying power density of solar spectrum ($0.1W/cm^2$) with area of solar cell on which solar illumination incident. For lateral NW structure this area is calculated by multiplying NW length excluding contact length with the diameter of NW. For vertical NW structure this area is the top cross section area of the solar cell. For multijunction solar cell this area is the cross section area of bottom solar cell.

1.4 Recombination Losses

The performance of solar cell is limited by the recombination process that occurs in the solar cell, which basically reduces the effective collection of charge carrier.

There are following recombination processes that limit the charge collection efficiency of a solar cell.

1.4.1 Shockley Read Hall Recombination

It is the dominant form of recombination mechanism in most of the solar cells. In this type of recombination due to the impurities present in the semiconductor an additional energy level is introduced within the forbidden energy gap. This energy level acts as a trap and captures electrons and holes, leading to recombination.

The relationship between recombination rate (U) (in unit of cm^{-3}/s) and trap density (N_t) (in unit of cm^{-3}) is given by relation [17].

$$U = \frac{\sigma_p \sigma_n v_{th} (pn - n_i^2) N_t}{\sigma_n \left[n + n_i \exp\left(\frac{E_t - E_i}{kT}\right) \right] + \sigma_p \left[p + n_i \exp\left(\frac{-(E_t - E_i)}{kT}\right) \right]} \quad (1.13)$$

Where,

σ_p = hole capture cross-section, n_i = intrinsic carrier density, v_{th} = thermal velocity
 σ_n = electron capture cross-section, E_i = intrinsic energy level, N_t = trap density

1.4.2 Band to Band Recombination

It is a radiative form of recombination in which an electron from conduction band recombines with the hole in the valence band with emission of energy [18]. Band to band recombination mainly occurs in direct band gap semiconductors. The probability of occurrence of this form of recombination in indirect band gap semiconductor is very low.

1.4.3 Auger Recombination

This type of recombination occurs in heavily doped semiconductors. In this recombination mechanism hole from the valence band recombines with the electron in the conduction band. The excess energy released during this recombination is absorbed by the neighboring electron in the conduction band, which then goes to some higher energy level and then again falls back to the conduction band with release of energy [18].

The Figure 1.4 shows all three kinds of recombination discussed above.

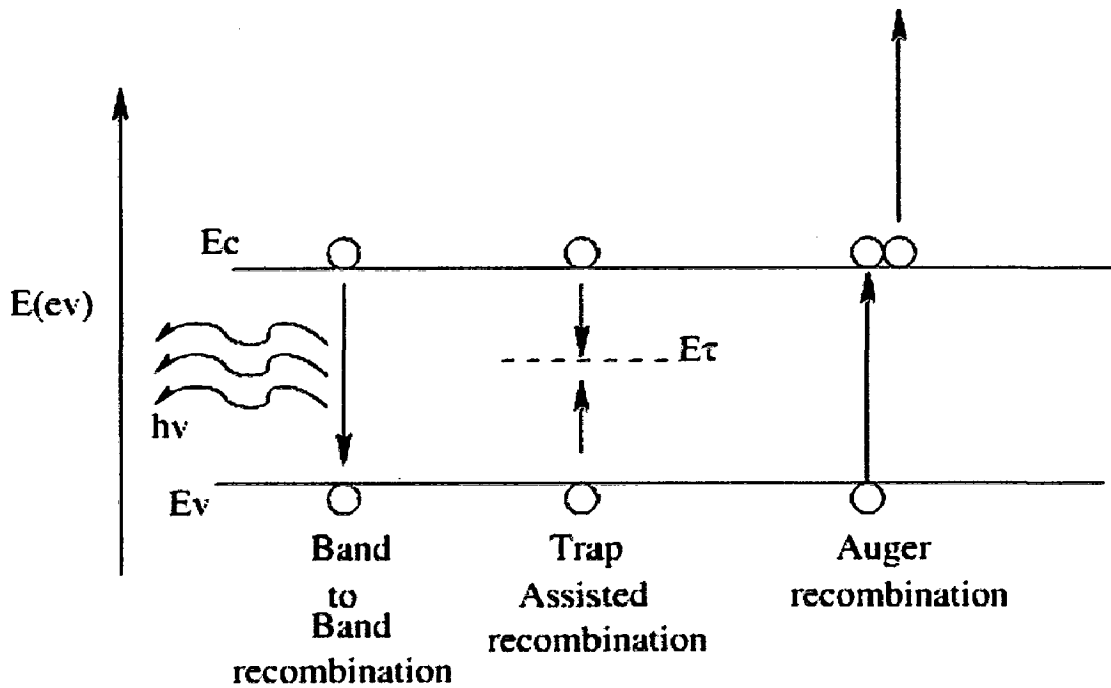


Figure 1.4 Schematic of different kind of recombination in a typical solar cell [18].

1.4.4 Surface Recombination

Because of abrupt termination of crystal structure, semiconductor surface has large number of dangling bonds. These dangling bond acts as recombination centers for charge carriers. Carriers generated near the surface fall in to these dangling bonds and gets recombine.

1.5 Multijunction Solar Cells Concept

With a traditional single junction solar cell, much of the incident light energy is not converted into electricity. If an incident photon has less energy than the semiconductor bandgap, the photon cannot be absorbed since there is not enough energy to excite an electron from the conduction band to the valence band. Therefore, none of the light with less energy than the semiconductor bandgap is used in the solar cell. If an incident photon has more energy than the bandgap, the excess energy will be lost in the form of heat.

Figure 1.5 shows the schematic of the photons that are absorbed in GaAs solar cell; on right, a plot showing the solar spectrum (in black) and the power converted by the GaAs cell (shaded green area). The maximum theoretical efficiency of this solar cell is 30% [20].

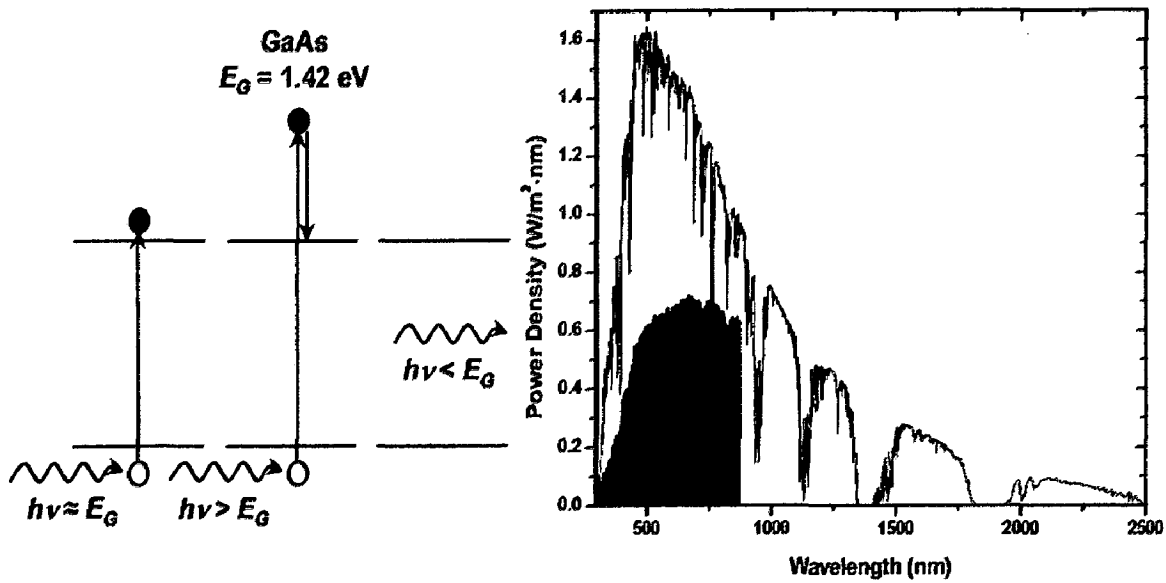


Figure 1.5 On left, a schematic of photon absorption in GaAs Solar cell; on right solar spectrum (in black) and power converted by GaAs solar cell (shaded area) [20].

The main idea of getting higher efficiency through utilizing the full solar spectrum is splitting the incoming energy spectrum into multiple segments, each of which are treated separately to enable more efficient charge collection. One idea of splitting the spectrum is to build the solar cell out of multiple semiconductor materials, and therefore multiple semiconductor materials, and therefore multiple band gaps. The materials have to be stacked in order of descending band gap since each material is only transparent to those photons with energies less than the band gap.

For connecting different cell pn-tunnel junction is used. The tunnel junction provides a low resistance connection between the p-type base of the upper cell and the n-type emitter of the lower cell. Tunnel diode must be designed such that the operating current of the device is below the peak tunneling current of tunnel junction.

The Figure 1.6 shows a schematic of the photons that are absorbed in a multijunction solar cell. The plot on right shows the solar spectrum (in black) and the power converted by each of four subcells (the shaded area). The maximum theoretical efficiency of this device is 55% [20].

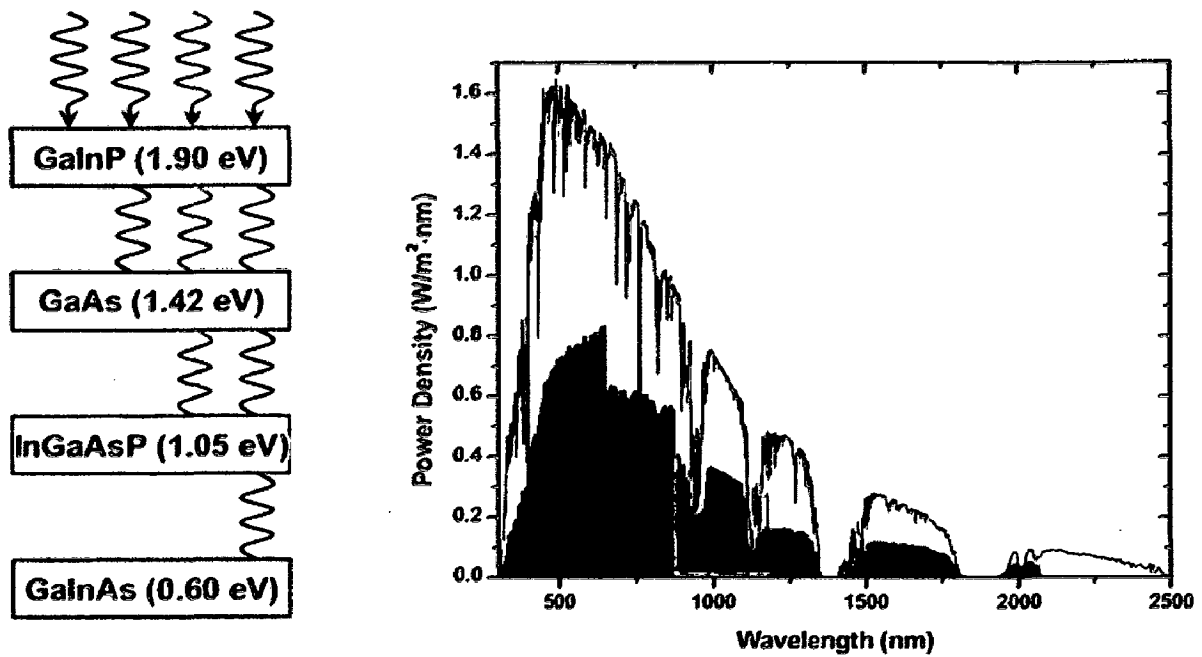


Figure 1.6 On left, a schematic of photons that are absorbed in four junction solar cell; on right, a solar spectrum (in black) and power converted by each of four sub cells (shaded regions) [20].

The inherent requirement of the multijunction solar cell is that the device has only two terminals. Therefore, one cell often limits performance of the entire device. To avoid this all the cells would ideally be current matched such that current produced in each sub cell is the same [20].

Chapter 2

Literature Review

2.1 Current Photovoltaic Technology

In recent years, tremendous emphasis is made to make the solar cell device, which is cost effective as well as giving high efficiency. For that reason nanostructure materials have been extensively explored for photovoltaic devices. Specifically NW devices have been studied experimentally and computationally [21-23]. The use of NW in solar cell has been tried like in dye-sensitized solar cell [24], polymer based solar cell and hybrid organic and inorganic solar cell [25].

There has been significant work on the use of metal oxide wires in dye-sensitized solar cell (DSSC) configurations [26], although a number of studies have also used metal oxide NWs as charge collectors in hybrid organic/inorganic solar cells. Some novel structures are also been tried like single-crystalline n-CdS nanopillars, embedded in polycrystalline thin films of p-CdTe [27] and vertically aligned p-type single-crystalline GaN nanorod arrays on n-type Si for heterojunction photovoltaic cells [28], to enable high absorption of light and efficient collection of the carriers.

In addition, silicon NWs have also been used to change the reflective properties of silicon solar cells [16]. Large emphasis is made on growing NWs on different substrate like glass, aluminum [4]. For getting the high efficiency using the silicon NWs grown using VLS method, research is going around the world to make them defect free and catalyst contamination free [14-15].

Conversion efficiency as high as 23% has been achieved with planar single junction silicon solar cell [29]. While, solar cell having 41% conversion efficiency has been demonstrated using multijunction concept [30].

The highest efficiency reported for vertical NW solar cell is around 6% [27] with CdS/CdTe structure. For lateral NW solar cell the best reported efficiency is around 4% with silicon co-axial p-i-n structure [9].

2.2 Current Limitations of Planar Junction Solar Cells

In planar junction solar cells minority carrier diffusion length must be long enough to allow for effective collection of photo generated charge-carriers generated deep inside the structure. Thus due to this reason the material needed for fabricating planar junction solar cell must be very pure, which makes planar junction solar cells bit expensive.

Figure 2.1 shows the schematic of a conventional planar solar cell. Conventional solar cell structure has requirement that when a photon of energy $h\nu$ generates an electron-hole pair in the p-type base of the solar cell, the cell thickness L must be greater than its optical thickness ($1/\alpha$), and the minority-electron diffusion length L_n must be long enough that any optically generated minority carrier can reach the pn-junction before recombining.

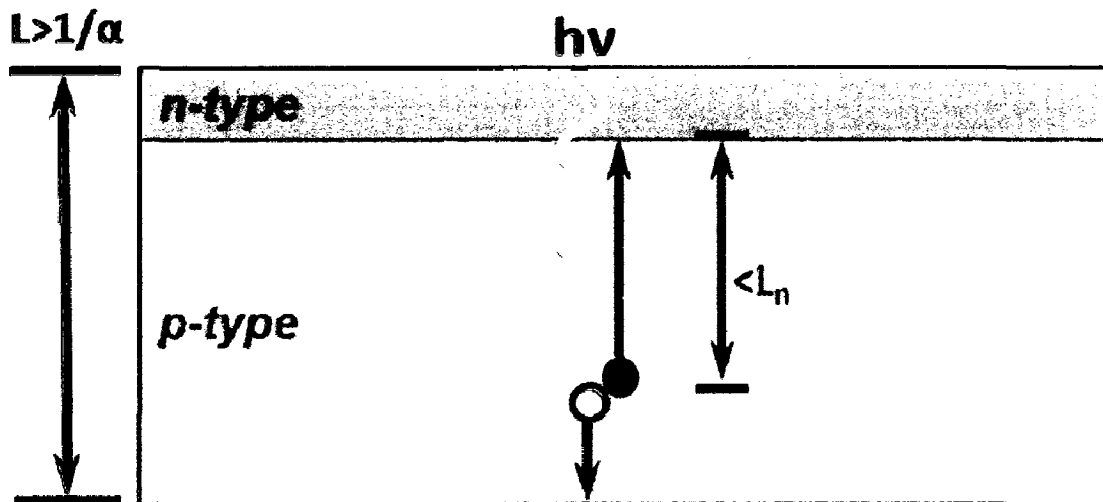


Figure 2.1 Schematic of conventional planar junction solar cell [31].

Inexpensive candidate materials for use in photovoltaic application generally have high density of defects, resulting in low minority-carrier diffusion length [29]. The use of such low diffusion-length materials as the absorbing base in conventional planar p-n junction solar cell geometry results in devices having a carrier collection limited by minority-carrier diffusion in the base region. Increasing the base thickness in such a cell will therefore produce more light absorption but will not results in an increase in device efficiency [10].

To overcome this problem a widespread attention is currently focused on new types of materials and structures for photovoltaic devices, such as polymer, dye sensitized and

NW based solar cells. Among them, silicon NW based solar cells are seriously considered as potential candidates for the next generation solar cells.

2.2 Advantages of NW Based Solar Cells

2.2.1 Defect Density Tolerance

A NW with pn-junction in radial direction can provide the solution to the problem of requirement of ultra pure material in solar cell by making the solar radiation absorption and charge carrier transport in orthogonal direction. Each individual pn-junction NW could be long enough to absorb the maximum part of solar spectrum, but also thin enough to allow effective carrier collection.

Figure 2.2 shows the schematic of NW based pn-junction solar cell. Here device requirement is that when a photon of energy $h\nu$ generates an electron hole pair in the p-core of NW, the wire length L must be greater than its optical thickness. But low minority electron diffusion length L_n can be tolerated because radius of the NW is very small, which makes the collection of charge carriers having low diffusion length possible.

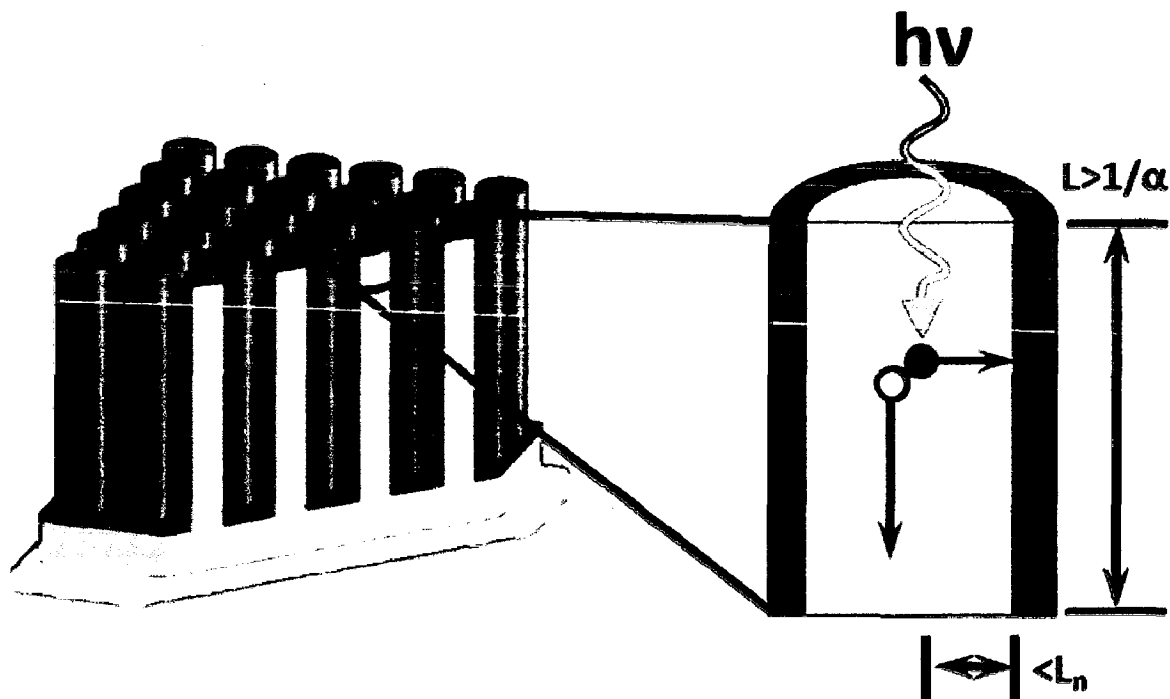


Figure 2.2 Schematic of NW based pn junction solar cell [31].

2.2.2 Light Scattering Effect

Solar cell based on NW array is shown to have enhanced light absorption because of scattering [28]. Figure 2.2.2 shows the schematic of NW array with light scattering effect. As the light travels through the NW array, it gets reflected by the NWs in turns increasing scattering and hence absorption, which eventually increases solar cell performance. The scattering of light in NW array is angle dependent as depicted in Figure 2.2.2. This makes the NW array solar cell performance angle dependent.

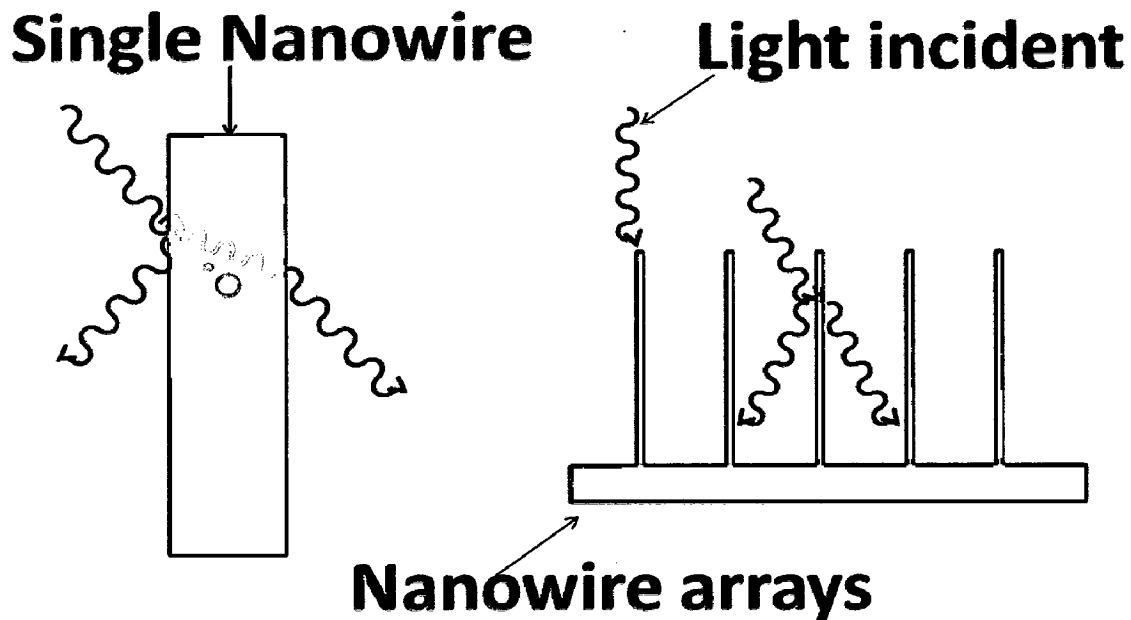


Figure 2.3 Schematic of NW array solar cell with light scattering effect.

2.2.3 Light Trapping Effect

It has been reported that there is a strong enhancement of the light absorption in single co-axial NW of silicon core/dielectric shells [13]. It has been found that there is a strong light trapping in silicon core because of the presence of dielectric shells. This enhancement in light trapping is basically due to the off-resonance enhancement, which strongly depends upon the core radius, the shell thickness, and the shell refractive index.

Figure 2.4 shows the schematic coaxial NW, where yellow (blue) stands for silicon core (shell), m_0 (air), m_1 (shell) and m_2 (core) are the refractive index.

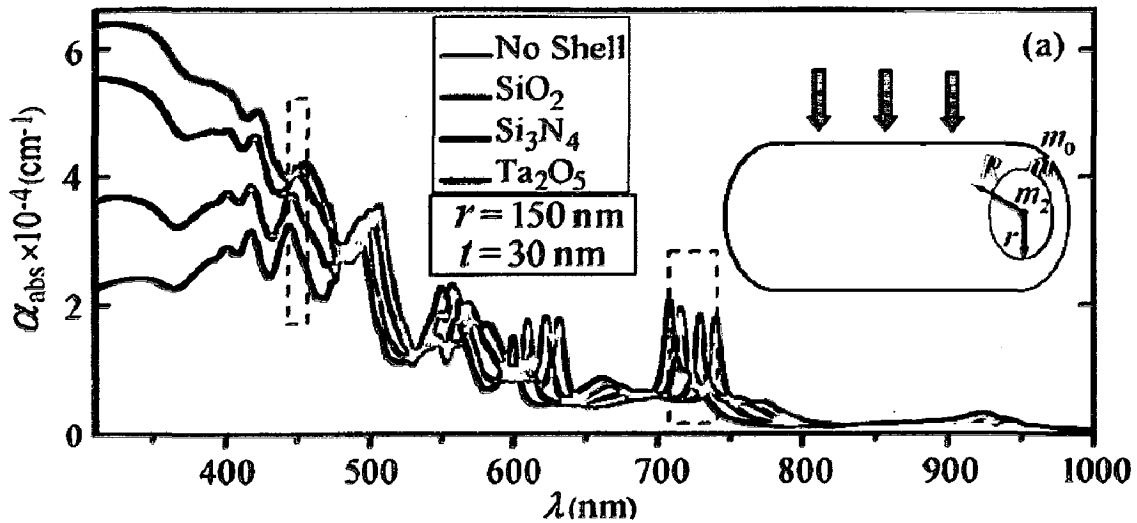


Figure 2.4 Schematics of coaxial NW with light trapping effect [13].

2.2.4 High Surface Area

NW has high surface area, although high surface area is not good for solid state solar cell because it increases the surface recombination, which degrades solar cell performance. But in case of dye-synthesized solar cell this high surface is useful and provide direct pathway for rapid collection of charge carrier generated throughout the solar cell [1-2].

2.2.5 Wider Range of Materials/Heterostructures

Another advantage of using NWs is that wider range of materials can be used in fabricating multijunction solar cells [22]. This is because NWs can withstand higher stain as compare to thin film, which allows us to use the different combination of materials to fully utilize the solar spectrum.

2.2.6 High Built-in Electric Field

NW structure has higher built-in electric field that arises because of its radial geometry. This higher electric field as compare to its planar counterpart plays, as will be discussed in chapter 4 and 5, very important role in efficient and rapid collection of generated electron-hole pairs.

Chapter 3

Simulation Tools and Methodology

3.1 Introduction to Device Simulation

Device simulations can be thought of as virtual measurements of the electrical behavior of a semiconductor device, such as a transistor or diode. The device is represented as a meshed finite-element structure. Each node of the device has properties associated with it, such as material type and doping concentration. For each node, the carrier concentration, current densities, electric field, generation and recombination rates, and so on are computed.

Technology Computer-Aided Design (TCAD) simulation tool by SYNOPSIS is used in this project.

3.2 Sentaurus Structure Editor

Sentaurus structure editor is a 2D and 3D device editor. It has two distinct operational modes: 2D structure editing and 3D structure editing and is used to build 2D and 3D device structures.

From the GUI, 2D and 3D device models are created geometrically using 2D or 3D primitives such as rectangles, polygons, cuboids, cylinders, and spheres.

The GUI of sentaurus structure editor features a command-line window, in which sentaurus structure editor prints script commands corresponding to the GUI operations. Doping profiles and meshing strategies are defined interactively. All doping and meshing options of the mesh generation tools Sentaurus Mesh, Mesh, and Noffset3D are supported.

Sentaurus Mesh is a modular delaunay 2D and 3D mesh generator that can create both axis-aligned and tensor meshes to be used in simulators that use the box discretization or finite-difference time-domain (FDTD) methods.

The mesh generator Noffset3D is fully unstructured and pays special attention to mesh elements near material interfaces.

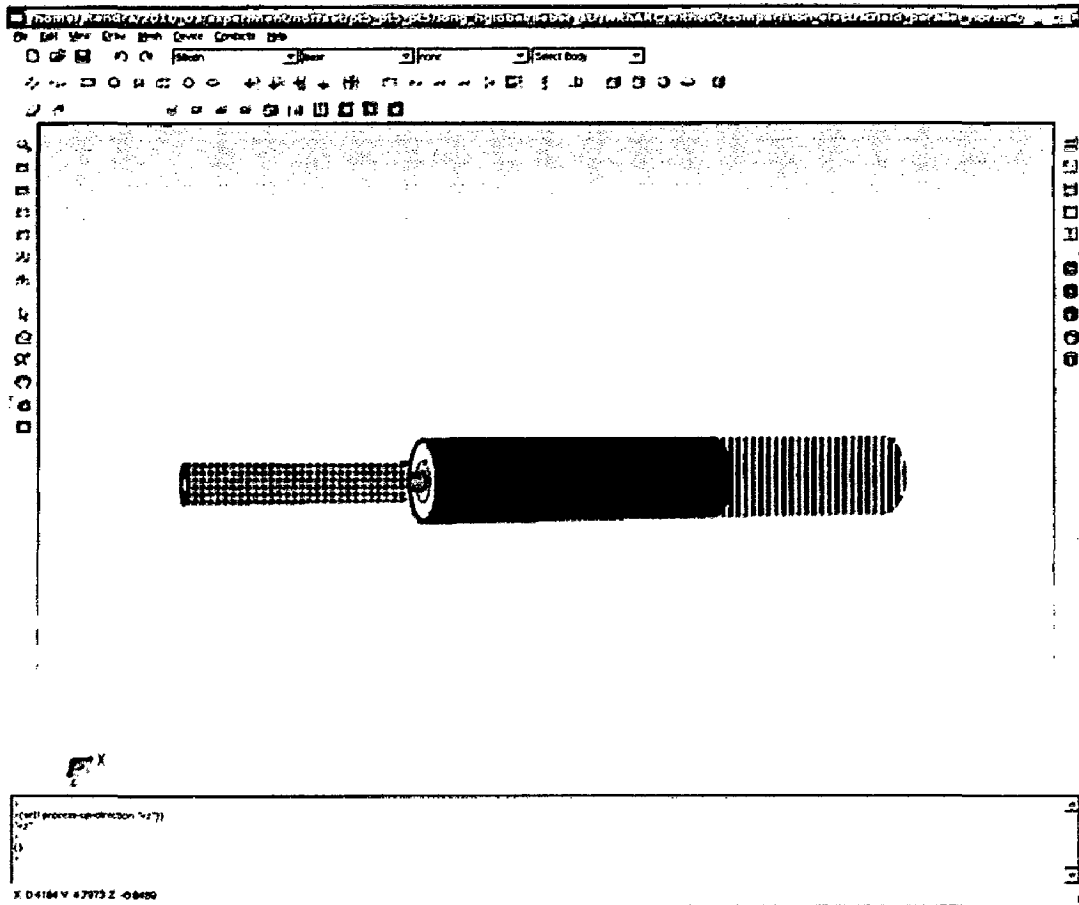


Figure 3.1 A typical sentaurus structure editor.

3.3 Sentaurus Device

Sentaurus device simulates the electrical, thermal and optical characteristics of semiconductor devices. It handles 1D, 2D, and 3D geometries, mixed-mode circuit simulation with compact models, and numeric devices. It contains a comprehensive set of physical models that can be applied to all relevant semiconductor devices and operation conditions.

A typical command file of sentaurus Device consists of several command sections, with each section executing a relatively independent function. The default extension of the command file is `_des.cmd`, for example, `n1_des.cmd`.

The command file typically contains the following sections

(a) *File Section:* It consists of input, output, parameter, doping and grid (generated after meshing) files.

(b) *Electrode Section*: It consists of electrode name given during structure generation. We have used onp for contact on p-core and on1 for contact on n-shell.

(c) *Physics Section*: It consists of the models that are being used in simulation. We have included the models like SRH recombination model, Auger recombination, doping dependent mobility and surface recombination model.

(d) *Plot Section*: This includes the different device parametric values, which are to be saved during simulation such as electric field, mobility, charge carrier velocity, current etc.

(e) *Math Section*: It includes the different mathematical algorithms, which are to be used for successful simulation.

(f) *Solve Section*: It consists of statements for solving coupled Poisson electron hole equations and the quasi-stationary blocks. These quasi-stationary blocks are used to bias and sweep an electrode with voltage or current value. It also solves for coupled Poisson electron hole equations at each simulation point.

Figure 3.2 shows the input and output file flow in sentaurus device.

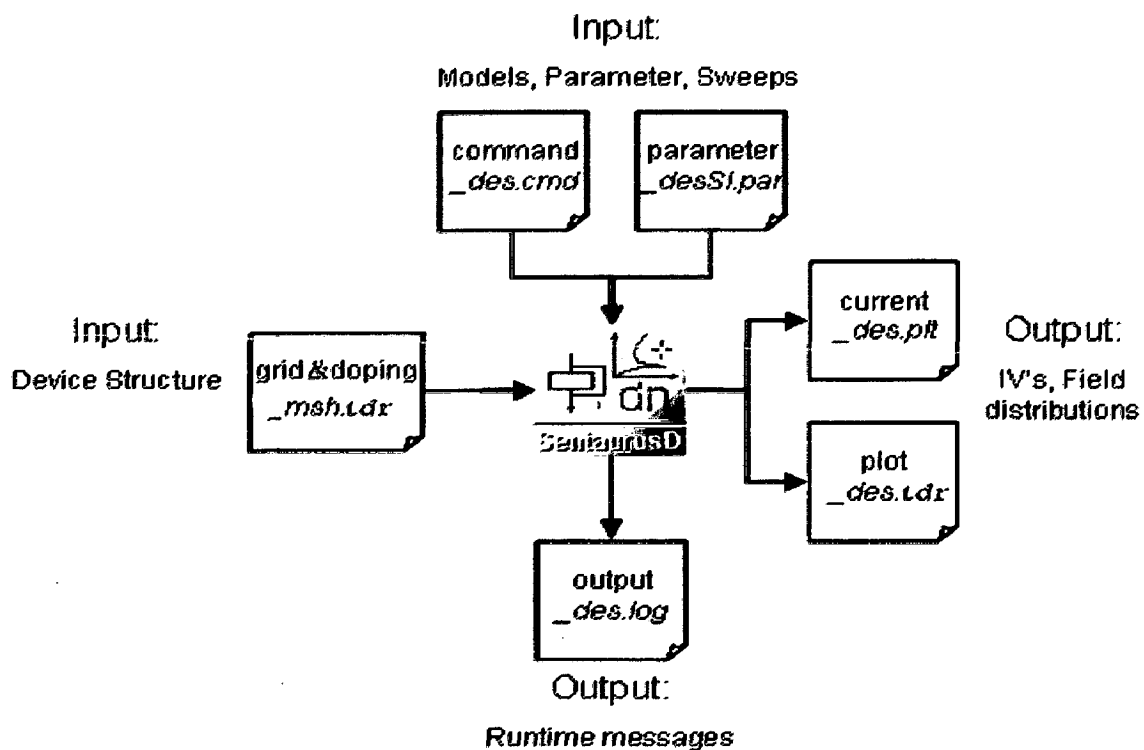


Figure 3.2 Schematic of input and output file flow in sentaurus device [32].

3.4 Tecplot SV

Tecplot SV is a plotting tool with extensive 2D and 3D capabilities for visualizing data from simulations and experiments. It represents state-of-the-art scientific visualization.

Tecplot SV can extract slices of data along the coordinate axes or user-defined lines of a 2D device, obtain 2D cross sections of 3D devices, and perform mathematical operations on the extracted data.

In addition, it is used to explore and analyze data, to produce informative 2D and 3D views, to create presentation-quality plots and animations.

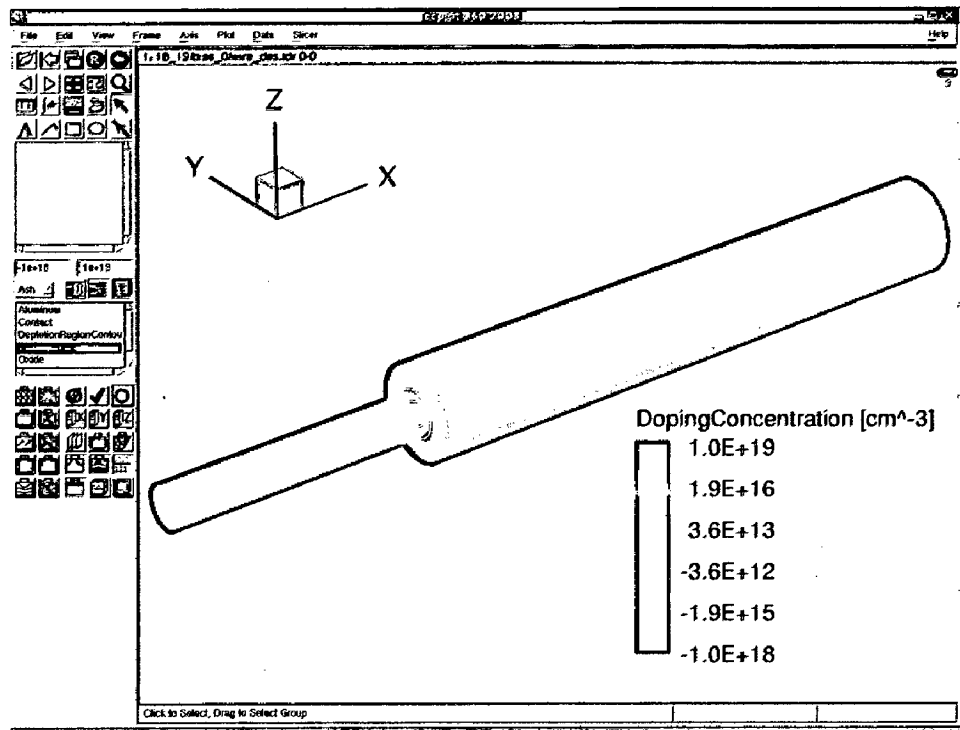


Figure 3.3 A typical tecplot of sentaurus device.

3.5 Inspect

Inspect is a versatile tool for efficient viewing of xy plots, such as doping profiles and I-V curves. Inspect extracts parameters, such as V_{oc} , and I_{sc} , from the respective xy plot. A script language and a library of mathematical functions allow us to compute with curves, and to manipulate and extract data from simulations.

Inspect features a large set of mathematical functions for curve manipulation, such as differentiation, integration, and find the minimum and maximum.

Chapter 4

Built-in Electric Field Modeling

4.1 Electric Field Modeling inside PIN-NW Structure

We have modeled the electric field inside NW along the radial direction as shown in Figure 4.1, which shows the cross section of NW PIN diode. For deriving electric field expression, we have used the abrupt depletion region approximation. In modelling equation we do not consider the electric field that will penetrate into the neutral region of the structure.

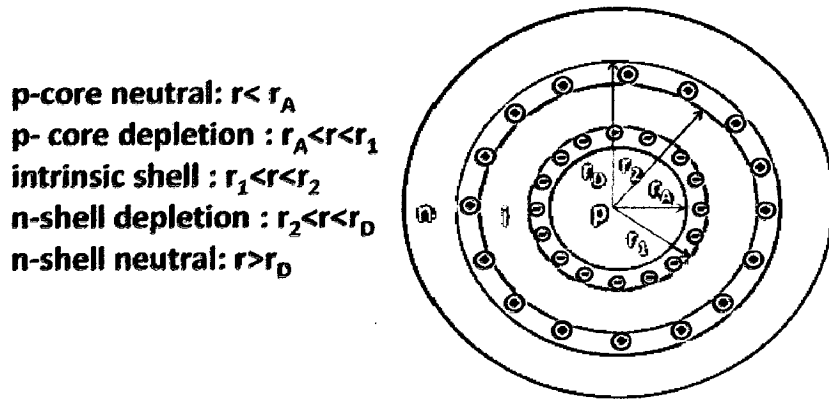


Figure 4.1 Cross section of radial junction PIN diode

Electric field in radial structure is calculated by solving Poisson's equation in cylindrical co-ordinates [33]

$$\frac{1}{r^2} \frac{d}{dr} [r^2 E(r)] = \frac{\rho(r)}{\epsilon} \quad (4.1)$$

Equivalently equation (4.1) can be written as

$$E(r) = \frac{1}{r} \int \frac{r\rho(r)}{\epsilon} dr + \frac{c}{r} \quad (4.2)$$

Where ρ is charge density, given as

$$\rho(r) = \left\{ \begin{array}{ll} 0 & r < r_A \\ -qN_A & r_A < r < r_1 \\ 0 & r_1 < r < r_2 \\ qN_D & r_2 < r < r_D \\ 0 & r > r_D \end{array} \right\} \quad (4.3)$$

(a) In p-core neutral region

Solution of equation (4.2) in p-core neutral region is

$$E(r) = \frac{c_1}{r} \quad (4.4)$$

Constant c_1 is found by using the boundary condition

$$\text{for } r < r_A, \quad E(r) = 0 \quad (4.5)$$

Which give $c_1 = 0$.

On substituting the constant c_1 value in equation (4.4), we get electric field value in p-core neutral region, which is 0.

(b) In p-core depletion region

Solution of equation (4.2) in this region is

$$E(r) = -\frac{1}{r} \left(\frac{qN_A r^2}{2\epsilon} \right) + \frac{c_2}{r} \quad (4.6)$$

Constant c_2 is found by using boundary condition

$$\text{at } r = r_A, \quad E(r_A) = 0 \quad (4.7)$$

Which give c_2 as

$$c_2 = \frac{qN_A r_A^2}{2\epsilon} \quad (4.8)$$

On substituting constant c_2 value in equation (4.6), we get electric field in p-core depletion region

$$E(r) = -\frac{qN_A(r^2 - r_A^2)}{2\epsilon r} \quad (4.9)$$

(c) In intrinsic shell region

Solution of equation (4.2) in this region is

$$E(r) = \frac{c_3}{r} \quad (4.10)$$

Constant c_3 is found using boundary condition

$$\text{at } r = r_1, \quad E(r_1) = -\frac{qN_A(r_1^2 - r_A^2)}{2\epsilon r_1} \quad (4.11)$$

Which give c_3 as

$$c_3 = -\frac{qN_A(r_1^2 - r_A^2)}{2\epsilon} \quad (4.12)$$

On substituting constant c_3 value in equation (4.10), we get electric field in intrinsic shell region

$$E(r) = -\frac{qN_A(r_1^2 - r_A^2)}{2\epsilon r} \quad (4.13)$$

(d) In n-shell depletion region

Solution of equation (4.2) in this region is

$$E(r) = \frac{1}{r} \left(\frac{qN_D r^2}{2\epsilon} \right) + \frac{c_4}{r} \quad (4.14)$$

Constant c_4 value is found using boundary condition

$$\text{at } r = r_2, \quad E(r_2) = -\frac{qN_A(r_1^2 - r_A^2)}{2\epsilon r_2} \quad (4.15)$$

Which give c_4 as

$$c_4 = -\frac{qN_A(r_1^2 - r_A^2)}{2\epsilon} - \frac{qN_A r_2^2}{2\epsilon} \quad (4.16)$$

On substituting constant c_4 value in equation (4.14), we get electric field in n-shell depletion region

$$E(r) = -\frac{qN_A(r_1^2 - r_D^2)}{2\epsilon r} \quad (4.17)$$

(e) In n-shell neutral region

Solution of equation (4.2) in this region is

$$E(r) = \frac{c_5}{r} \quad (4.18)$$

Value of constant c_5 is found using boundary condition

$$\text{for } r > r_D, \quad E(r) = 0 \quad (4.19)$$

Which give c_5 as

On substituting the constant c_5 value in equation (4.18), we get electric field value in n-shell neutral region, which is 0.

$$E(r) = \begin{cases} 0 & r < r_A \\ -\frac{qN_A(r^2 - r_A^2)}{2r\epsilon} & r_A < r < r_1 \\ -\frac{qN_A(r_1^2 - r_A^2)}{2r\epsilon} & r_1 < r < r_2 \\ \frac{qN_D(r^2 - r_D^2)}{2r\epsilon} & r_2 < r < r_D \\ 0 & r > r_D \end{cases} \quad (4.20)$$

4.2 Electric Field Modeling inside PIN-Planar Structure

Similarly the electric field for PIN planar junction can be obtained with appropriate boundary conditions [34].

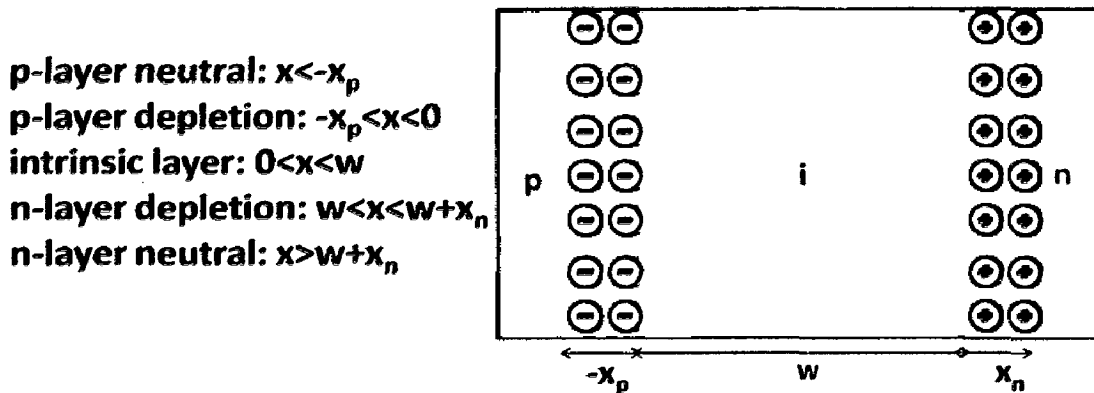
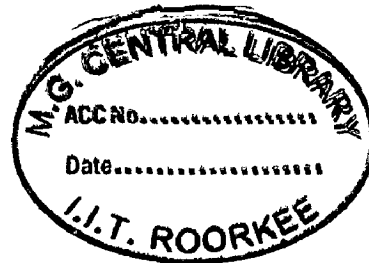


Figure 4.2 Cross section of planar junction PIN diode

The electric field in planar structure can be calculated by solving Poisson's equation in rectangle co-ordinates

$$\frac{\partial E(x)}{\partial x} = \frac{\rho}{\epsilon} \quad (4.21)$$



Equivalently equation (4.21) can be written as

$$E(x) = \int \frac{\rho(x) dx}{\epsilon} + c \quad (4.22)$$

Where ρ is charge density, given as

$$\rho(x) = \begin{cases} 0 & x < -x_p \\ -qN_A & -x_p < x < 0 \\ 0 & 0 < x < w \\ qN_D & w < x < w + x_n \\ 0 & x > w + x_n \end{cases} \quad (4.23)$$

On solving equation (4.22) and equation (4.23) with boundary condition, we get electric field in planar structure given as

$$E(x) = \begin{cases} -\frac{qN_A}{\epsilon} (x + x_p) & -x_p < x < 0 \\ -\frac{qN_A x_p}{\epsilon} & 0 < x < W \\ \frac{qN_D}{\epsilon} [x - (W + x_n)] & W < x < W + x_n \end{cases} \quad (4.24)$$

4.3 Modeled and Simulated Electric Field Comparison in Radial and Planar PIN-Structures

To do the comparative study of modeled and simulated efield, we have simulated a NW and planar structures with doping density of 10^{18} cm^{-3} and 10^{19} cm^{-3} in p and n region respectively. Figure 4.3 shows the comparison of modeled and simulated electric field for radial and planar structure.

Inside i-layer good matching is obtained between simulated and modeled value. We note that peak electric field in radial structure is 1.53 times higher than peak electric field in planar structure. This is the main reason that radial structure shows very good performance in terms of conversion efficiency over its planar counterpart as will be discussed in chapter 5. We have modeled and plotted electric field inside the radial and planar structures using equations (4.20) and (4.24) respectively. The values of parameters used in these equations are as follows

$$r_A = 3.78 \times 10^{-6} \text{ cm}, r_1 = 5 \times 10^{-6} \text{ cm}, r_2 = 1 \times 10^{-5} \text{ cm}, r_D = 1.007 \times 10^{-5} \text{ cm}, x_p = 6.29 \times 10^{-7} \text{ cm}, W = 1 \times 10^{-5} \text{ cm}, x_n = 6.29 \times 10^{-8} \text{ cm}, N_A = 10^{18} \text{ cm}^{-3}, N_D = 10^{19} \text{ cm}^{-3}.$$

Since our model does not consider the Debye length effect, hence modeled equations do not model the electric field inside the quasi-neutral region of the structure.

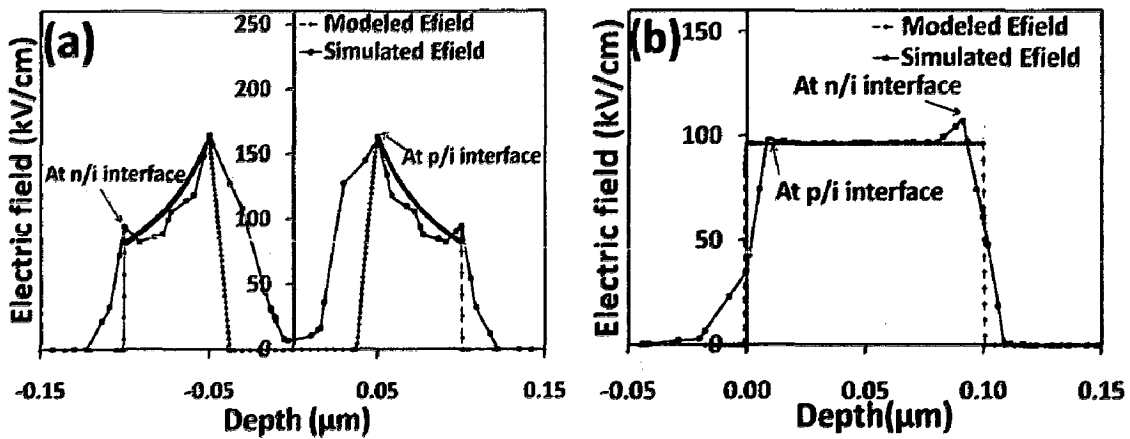


Figure 4.3 Modeled and simulated E-field (a) radial structure, (b) planar structure.

4.4 Electric Field Modeling inside PN-Nanowire Structure

Figure 4.4 shows the cross section of NW PN-diode. We have used the abrupt depletion region approximation for deriving electric field expression in NW structure as we have

used in the case of PIN structure. In modelling equation we do not consider the electric field that will penetrate the quasi-neutral region of the structure.

p-core neutral : $r < r_A$
p-core depletion : $r_A < r < r_j$
n-shell depletion : $r_j < r < r_D$
n-shell neutral : $r > r_D$

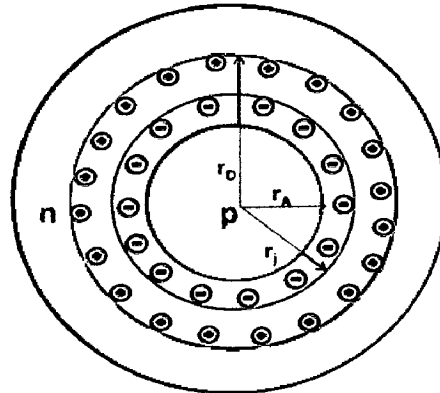


Figure 4.4 Cross section of radial junction PN diode.

Electric field in cylindrical structure is calculated by solving Poisson's equation in cylindrical co-ordinates

$$\frac{1}{r^2} \frac{d}{dr} [r^2 E(r)] = \frac{\rho(r)}{\epsilon} \quad (4.25)$$

Equivalently equation (4.25) can be written as

$$E(r) = \frac{1}{r} \int \frac{r \rho(r)}{\epsilon} dr + \frac{c}{r} \quad (4.26)$$

Where ρ is charge density, given as

$$\rho(r) = \begin{cases} 0 & r < r_A \\ -qN_A & r_A < r < r_j \\ qN_D & r_j < r < r_D \\ 0 & r > r_D \end{cases} \quad (4.27)$$

On solving equations (4.26) and (4.27) with boundary conditions $E(r) = 0$ for $r = r_A$ and $r = r_D$, we get electric field as

$$E(r) = \begin{cases} 0 & r < r_A \\ -\frac{qN_A(r^2 - r_A^2)}{2r\epsilon} & r_A < r < r_j \\ \frac{qN_D(r^2 - r_D^2)}{2r\epsilon} & r_j < r < r_D \\ 0 & r > r_D \end{cases} \quad (4.28)$$

4.5 Electric Field Modeling inside PN-Planar Structure

Similarly the electric field for PN planar junction can be obtained with appropriate boundary conditions as

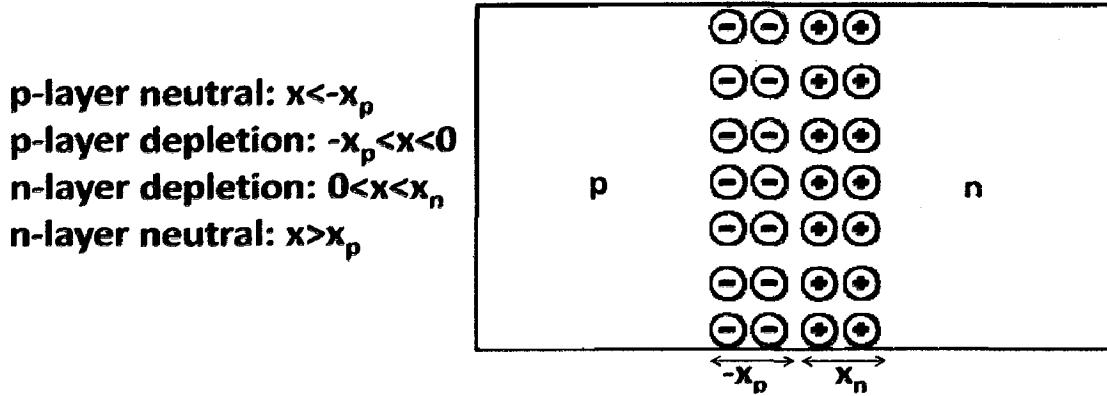


Figure 4.5 Cross section of planar junction PN diode.

The electric field in planar structure can be calculated by solving Poisson's equation in rectangle co-ordinates

$$\frac{\partial E(x)}{\partial x} = \frac{\rho}{\epsilon} \quad (4.28)$$

Equivalently equation (4.28) can be written as

$$E(x) = \int \frac{\rho(x)dx}{\epsilon} + c \quad (4.29)$$

Where ρ is charge density, given as

$$\rho(r) = \begin{cases} 0 & x < -x_p \\ -qN_A & x_p < x < 0 \\ qN_D & 0 < x < x_n \\ 0 & x > x_n \end{cases} \quad (4.30)$$

On solving equation (4.29) and equation (4.30) with boundary condition, we get Electric field in planar structure given as

$$E(x) = \begin{cases} -\frac{qN_A}{\epsilon}(x + x_p) & -x_p < x < 0 \\ \frac{qN_D}{\epsilon}[x - x_n] & 0 < x < x_n \end{cases} \quad (4.31)$$

4.6 Modeled and Simulated Electric Field Comparison in Radial and Planar PN-Structures

Figure 4.6 shows the comparison of modeled and simulated electric field for radial and planar structure respectively. We note that peak electric field at p/n-interface in radial structure is 1.33 times higher than that at p/n-interface in planar structure.

This is the main reason that radial structure shows very good performance in terms of conversion efficiency over its planar counterpart as will be discussed in chapter 6. We have modeled and plotted electric field inside the radial and planar structures using equations (4.28) and (4.31) respectively, with following parameter values.

$r_A = 9.038 \times 10^{-6}$ cm, $r_j = 9.50 \times 10^{-6}$ cm, $r_D = 9.962 \times 10^{-6}$ cm, $x_p = 3.4 \times 10^{-7}$ cm, $x_n = 3.4 \times 10^{-7}$ cm, $N_A = 10^{19}$ cm⁻³, $N_D = 10^{19}$ cm⁻³.

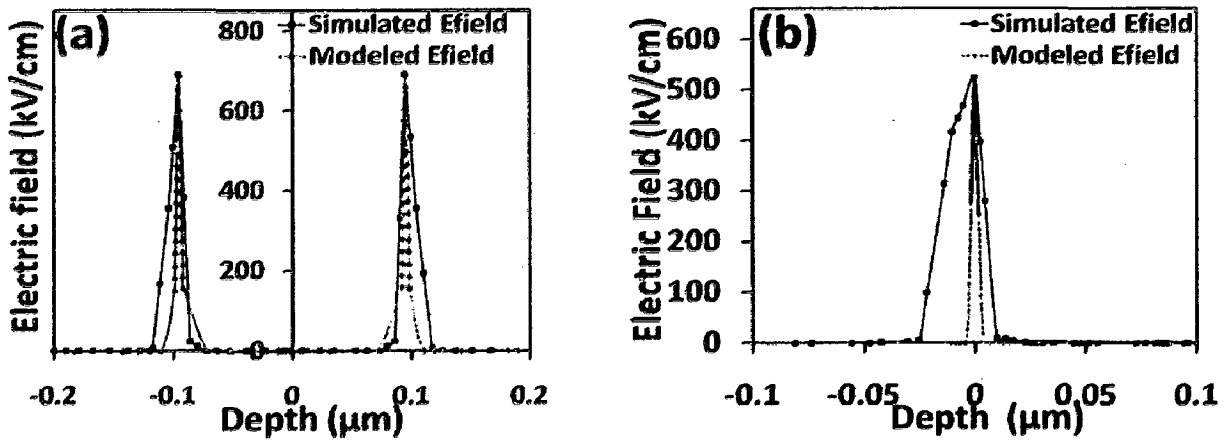


Figure 4.6 Modeled and simulated E-field (a) radial structure, (b) planar structure.

4.7 Summary

We have modeled and simulated the electric field inside PIN and PN junction NW structures along the radial direction. Very good matching is obtained between simulated and modeled value inside i-layer. We note that peak electric field at p/i interface in PIN-NW structure is 1.53 times higher than the peak electric field in planar structure for the doping density of 10^{18} cm⁻³ and 10^{19} cm⁻³ in p-core and n-shell respectively.

Similarly for PN-NW structure results show that for the doping density of 10^{19} cm⁻³ in p-core and n-shell, peak electric field in PN-NW structure at p/n-interface is 1.33 times higher than that at p/n-interface in planar structure.

Chapter 5

Lateral PIN-Nanowire Solar Cell

5.1 Structure Details

The co-axial PIN-NW structure studied in this work is shown in Figure 5.1. In this structure, exterior "shell" of the NW is n-type, interior "core" of NW is p-type and the middle shell is i-type. Aluminium metal contacts are made on interior p-core and on exterior n-shell. For surface passivation a 20 nm thick silicon oxide (SiO_2) layer is used on the outer surface of the structure.

For benchmarking purpose we have created a planar PIN-junction structure of same dimensions keeping width of planar structure equal to the diameter of radial structure.

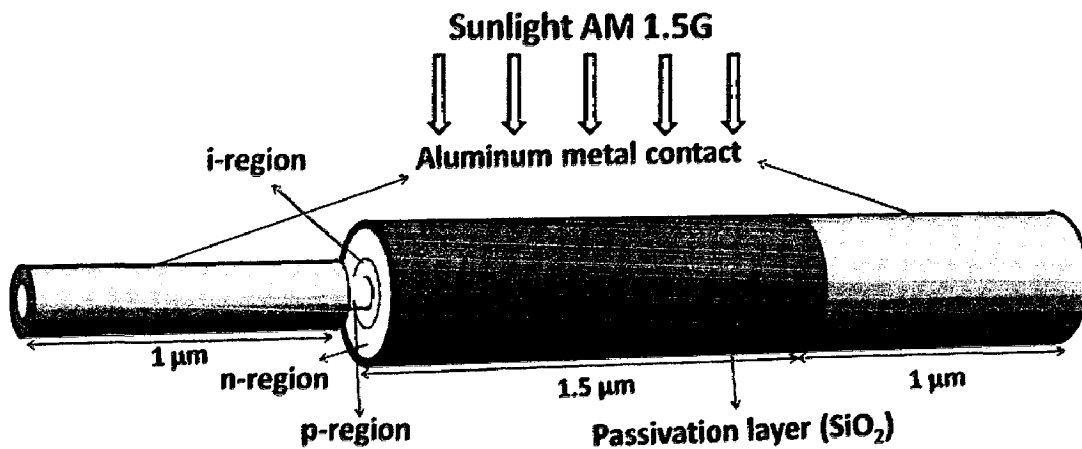


Figure 5.1 Structure of the co-axial NW PIN-junction solar cell.

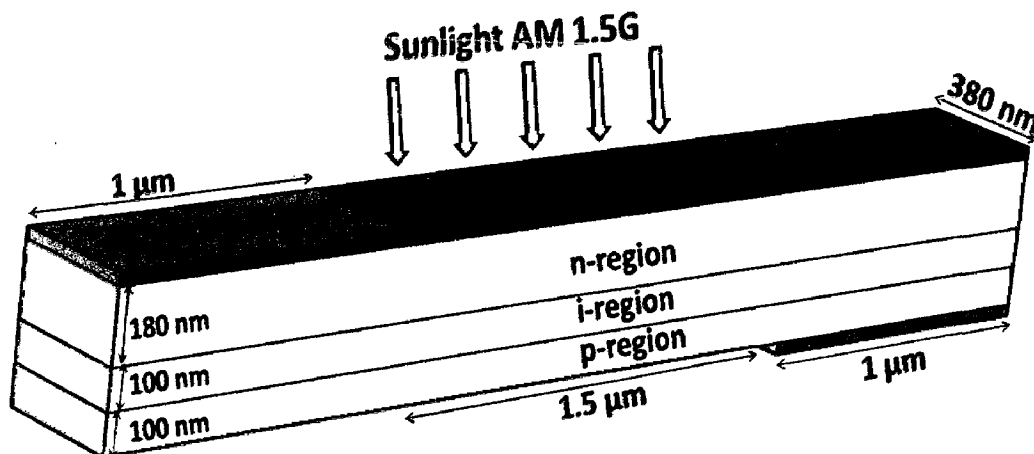


Figure 5.2 Structure of the planar PIN-junction solar cell.

Figure 5.2 shows the planar structure used for benchmarking. Standard A.M. 1.5G solar spectrum is used with light incident normally on the top surface as shown in Figures 5.1 and 5.2. In device simulation of implemented structure all important recombination statistics namely Shockley-Read-Hall recombination, Auger recombination, and surface recombination are incorporated. TCAD calculates optical generation rate in solar cell using raytracing model [32] and couples it with electrical simulation solving Poisson's and continuity equations.

Table 5.1 shows structural and device model parameters of un-optimized NW cell. Same parameters are also used for planar structure.

Table 5.1 Structure parameters of un-optimized lateral NW solar cell

Parameter	Value	Parameter	Value
Length of NW	1.5 μm	Oxide layer thickness	20 nm
p-core radius	50 nm	p-core doping density	10^{16} cm^{-3}
n-shell thickness	90 nm	n-shell doping density	10^{16} cm^{-3}
Intrinsic (i) shell thickness	50 nm	i-shell doping density	un-doped
Surface recombination velocity at silicon/ aluminium interface	10^5 cm^{-2}	Surface recombination velocity at silicon/ oxide interface	10^3 cm^{-2}
Electron capture cross section	10^{-15} cm^{-2}	Hole capture cross section	10^{-15} cm^{-2}

5.2 Structural Parameters Optimization

To optimize NW solar cell structure, we have evaluated I_{sc} , V_{oc} and conversion efficiency versus varying doping density and i-layer thickness curves.

The NW structure is optimized firstly by keeping p-layer doping constant and varying n-layer doping. Figure 5.3 shows the effect of n-layer doping variation on I_{sc} , V_{oc} and conversion efficiency for radial and planar structures. As doping density in n-layer increases recombination centers are increased, which results in decrease in I_{sc} for planar structure. But for radial structure because of its radial geometry and higher peak electric field, it has I_{sc} which continuously increases with increasing doping density.

As doping density of n-layer is increased, built-in potential increases, which in turns increase the V_{oc} . From Figure 5.3 best performance, in term of conversion efficiency for NW structure with n-layer doping density of 10^{19} cm^{-3} is obtained. At this doping density radial structure has conversion efficiency, which is 1.7 times higher than that of planar structure.

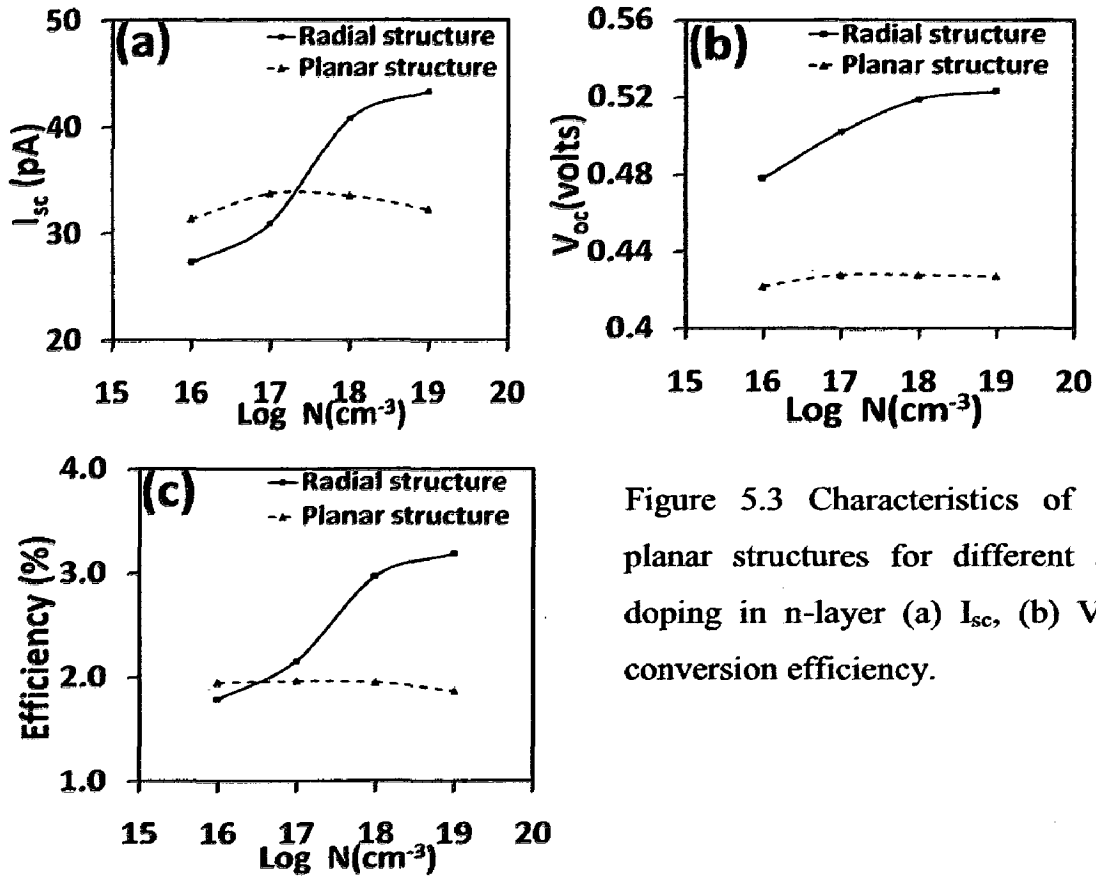


Figure 5.3 Characteristics of radial and planar structures for different amount of doping in n-layer (a) I_{sc} , (b) V_{oc} and (c) conversion efficiency.

Solar cell performance is limited by the carrier diffusion length which in turns depends upon the mobility. As doping density increases mobility of charge carriers decreases, which in turn reduces the charge carrier diffusion length [33].

Figure 5.4 shows the effect of p-layer doping variation on I_{sc} , V_{oc} and conversion efficiency for radial and planar structure. As n-layer already have very high doping density and hence in turns high efield, therefore increase in p-layer doping density has no effect on I_{sc} for both radial and planar structure.

With increase in doping density in p-layer minority carrier concentration decreases, which in turns decreases leakage current [17].

$$I_o = \frac{qAD_p p_{no}}{L_p} + \frac{qAD_n n_{po}}{L_n} \quad (5.1)$$

This reduction in leakage current will increase V_{oc} as indicated by equation (1.6). From simulation results the optimized value of p-core and n-shell doping density are 10^{18} cm⁻³ and 10^{19} cm⁻³ respectively. At above optimized values of p-core and n-shell doping

radial structure has 1.36 times higher conversion efficiency over planar structure as shown by Figure 5.4 (c).

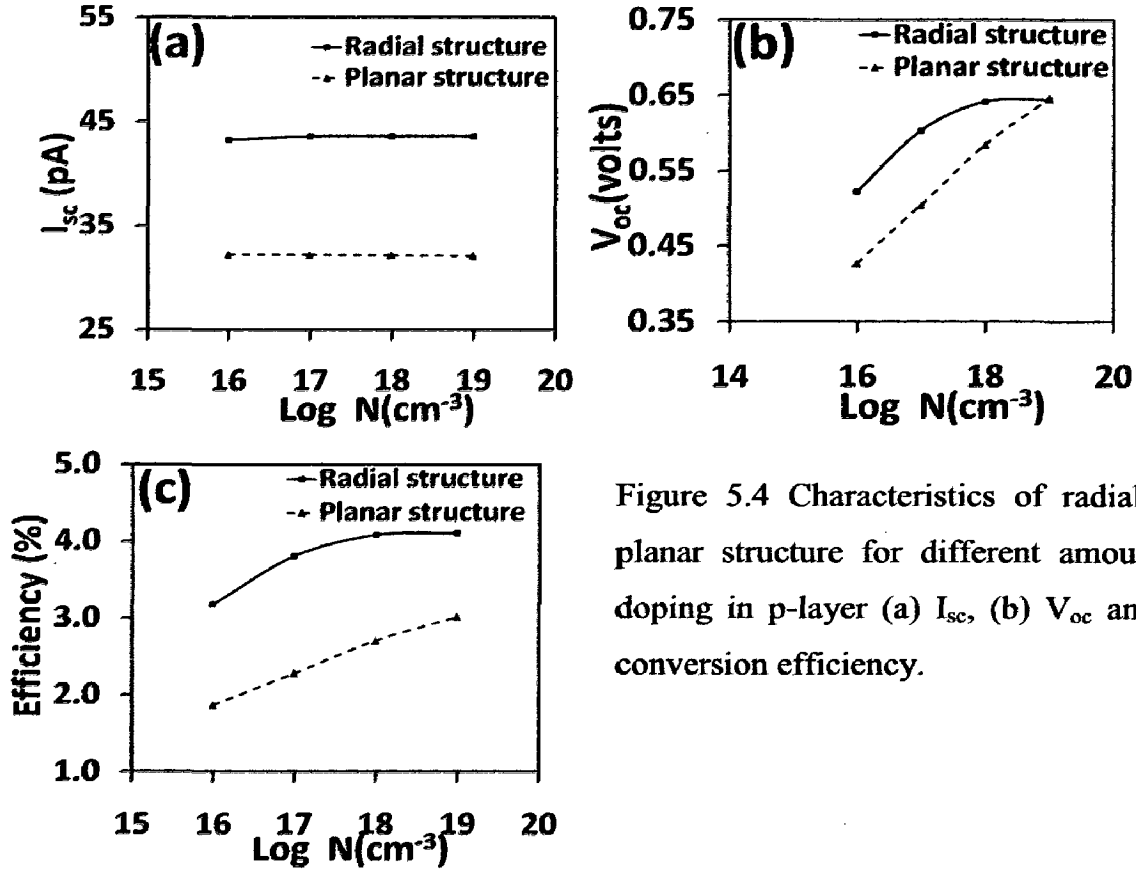


Figure 5.4 Characteristics of radial and planar structure for different amount of doping in p-layer (a) I_{sc} , (b) V_{oc} and (c) conversion efficiency.

Optimization of i-layer thickness is also done keeping optimized value of n and p layers doping density, which are 10^{18} cm⁻³ and 10^{19} cm⁻³ respectively. As i-layer thickness is increased, more and more light will get absorbed in i-layer of the structure, hence more electron hole pairs (EHPs) will be generated. This results in the enhancement in the I_{sc} as shown by Figure 5.5 (a).

For the case of V_{oc} as i-layer thickness increases leakage current increases [33]

$$I_o = qWA \frac{n_i}{2\tau} \quad (5.2)$$

Where W is the width of depletion region, τ is life time of carriers and n_i is intrinsic carrier concentration.

Because of this increase in leakage current, there is slight decrease in V_{oc} with increase in i-layers thickness as depicted by Figure 5.5 (b). From simulation results optimized value of NW i-layer thickness is found to be 80 nm. At this i-layer thickness

radial structure has 1.46 times higher conversion efficiency than its planar counterpart as shown by Figure 5.5(c).

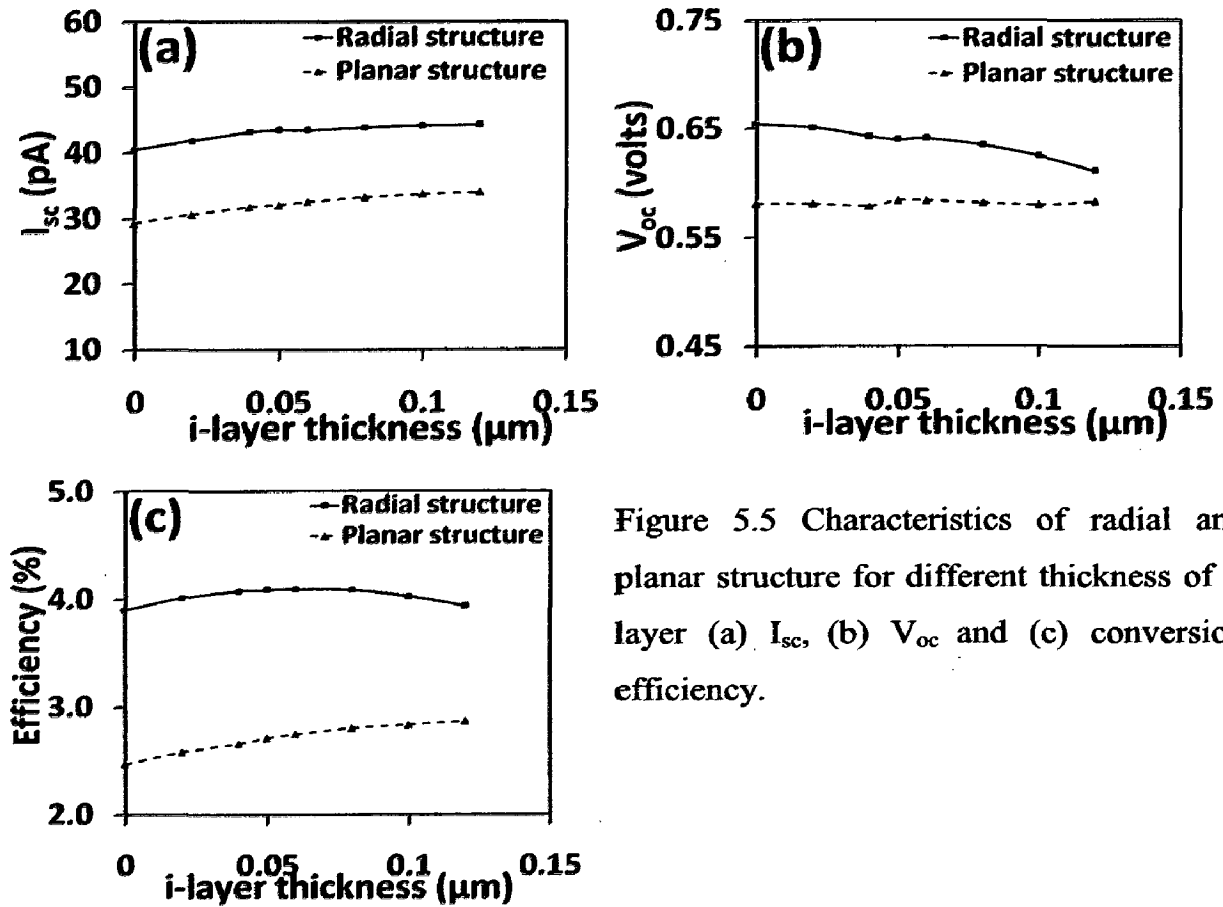


Figure 5.5 Characteristics of radial and planar structure for different thickness of i-layer (a) I_{sc} , (b) V_{oc} and (c) conversion efficiency.

One of the most important effects of having junction in radial direction is that even with low quality material it gives sufficiently high efficiency. To compare the performance of radial and planar structures with different amount of defect density present in it, we have intentionally introduced donor type defects at intrinsic energy level in i-layers of both radial and planar structures.

Figure 5.6 shows the effect of defect density on I_{sc} , V_{oc} and conversion efficiency for radial and planar structures.

We note from Figure 5.6 (a) that I_{sc} remains constant for both radial and planar structure as trap density increases. This is because both radial and planar structure has a dimension of order of 380 nm; hence the reduction of minority carrier diffusion length will not affect the I_{sc} current.

But overall radial structure has 1.3 times higher I_{sc} than planar structure because of its radial geometry. But in case of V_{oc} , since increasing trap density increase the recombination centers, which in turns increases recombination current resulting decrease in V_{oc} as shown by Figure 5.6 (b). At low defect density of about 10^{12} cm^{-3} radial structure shows 33.50% higher conversion efficiency and while at high defect density of 10^{18} cm^{-3} radial structure shows 118.60% higher conversion efficiency as compare to its planar counterpart.

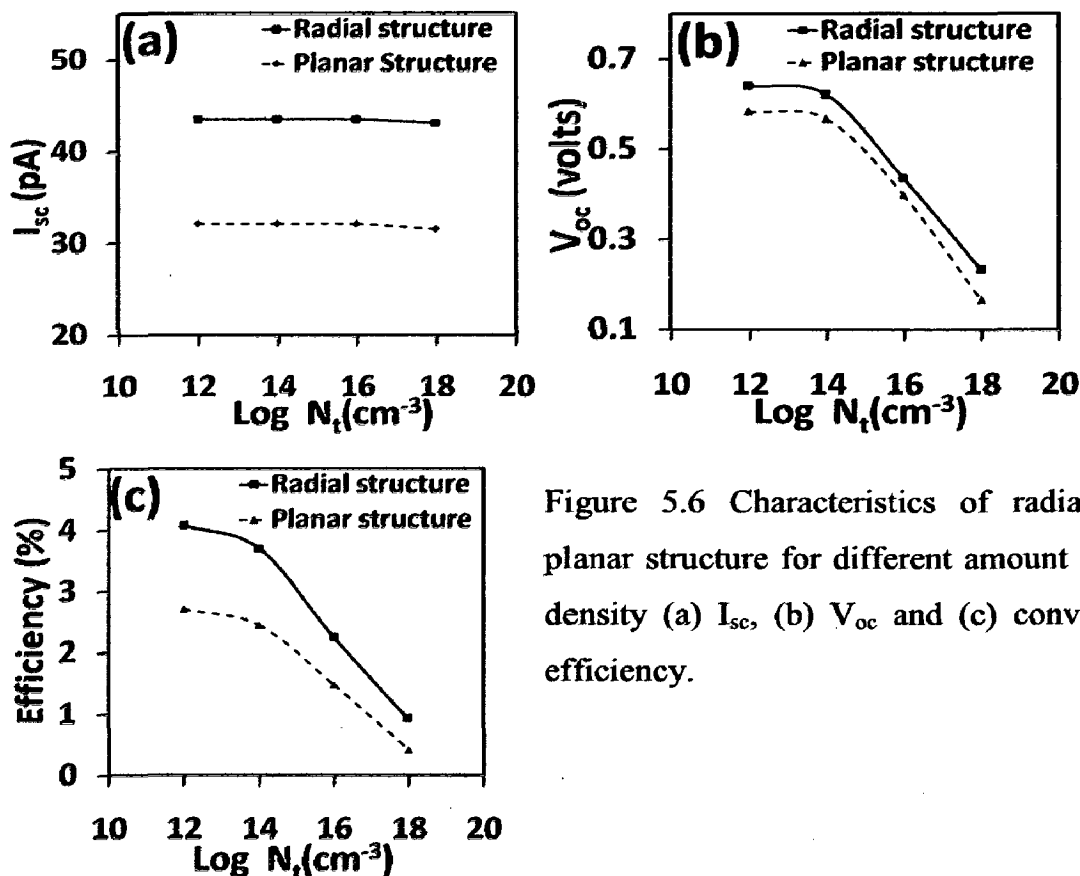


Figure 5.6 Characteristics of radial and planar structure for different amount defect density (a) I_{sc} , (b) V_{oc} and (c) conversion efficiency.

5.3 Illumination Angle Study

To study the effect of solar radiation incident angle on lateral NW solar cell performance, we have simulated NW structure with passivation oxide (SiO_2) layer for three different angles of solar radiation incident viz. 30° , 60° and 90° .

Figure 5.7 shows solar radiation incident angle effect on I_{sc} , V_{oc} and conversion efficiency for radial structure with and without oxide layer.

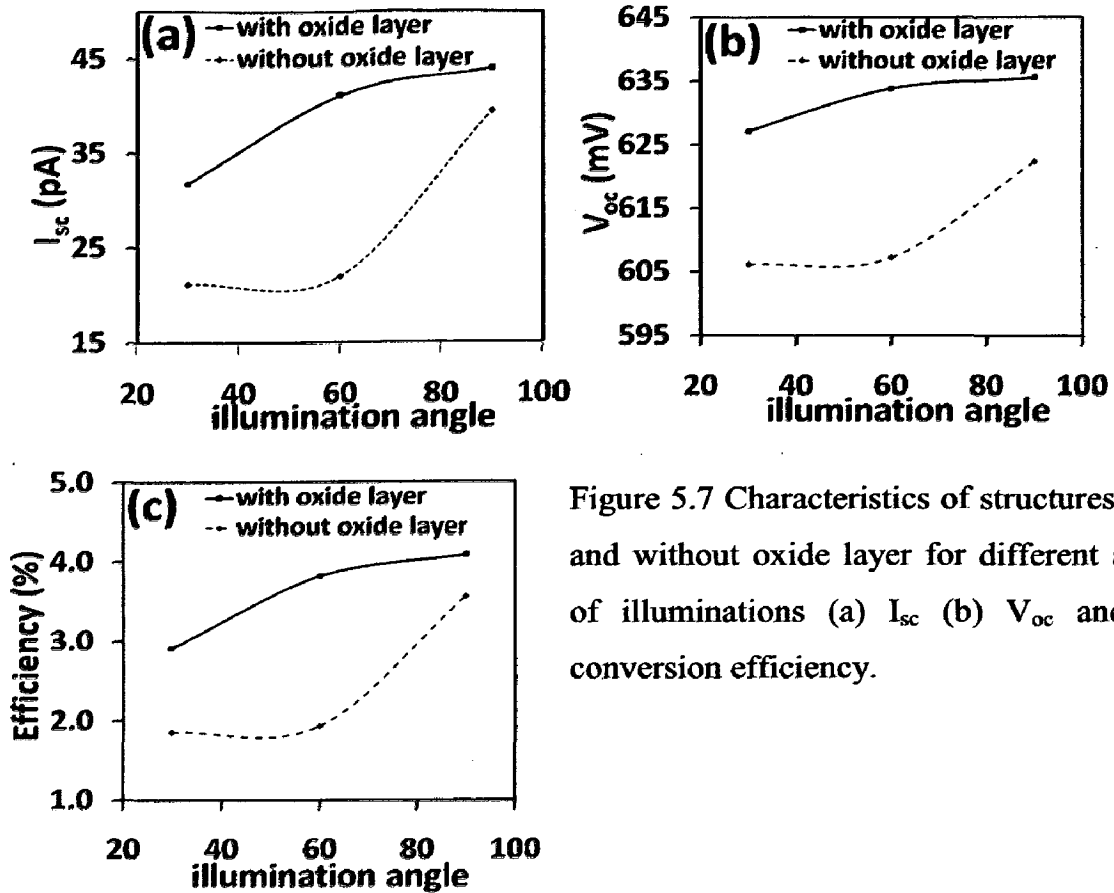


Figure 5.7 Characteristics of structures with and without oxide layer for different angle of illuminations (a) I_{sc} (b) V_{oc} and (c) conversion efficiency.

Our simulation result shows that with increase in incident angle solar cell conversion efficiency increases, with optimum angle of incident comes out to be 90°.

To find the behavior of NW cell at different angle of incident for different wavelength, we have calculated the EQE of NW structure with SiO_2 at different incident angle (Figure 5.8).

We have calculated the EQE using equation (5.3) given as

$$EQE = \frac{Ihc}{q\lambda I_0 S} \quad (5.3)$$

Where h is Plank's constant, c is the speed of light, λ is the wavelength, I_0 is the incident light intensity, I is the photogenerated current and S is the incident surface area.

It is found that with the increase in incident angle, EQE increases for smaller wavelength, while for higher wavelength EQE is almost same for all three different incident angles. This is because as the incident light wavelength increases absorption coefficient decreases due to which EQE decreases with increase in wavelength.

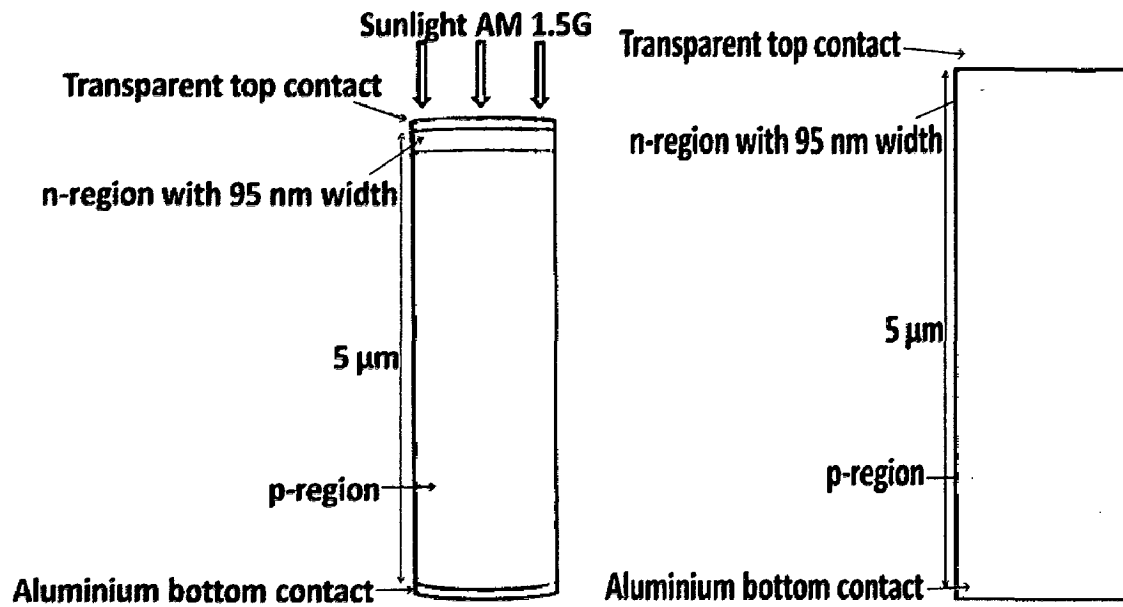


Figure 6.2 On left, 3D view of PN-planar junction solar cell structure used for bench marking, in this simulation study; on left, 2D cross section view of the same structure.

Table 6.1 shows structural and device model parameters of un-optimized vertical PN-NW cell. Same parameters are also used for planar structure.

Table 6.1 Structure parameters of un-optimized vertical NW solar cell

Parameter	Value	Parameter	Value
Length of NW	5 μm	Si_3N_4 layer thickness	20 nm
p-core radius	95 nm	p-core doping density	10^{16} cm^{-3}
n-shell thickness	95 nm	n-shell doping density	10^{16} cm^{-3}
surface recombination velocity at silicon/ Si_3N_4 interface	10^3 cm^{-2}	surface recombination velocity at silicon/ contact interface	10^5 cm^{-2}
Electron capture cross section	10^{-15} cm^{-2}	Hole capture cross section	10^{-15} cm^{-2}

6.1.2 Structural Parameters Optimization

First of all, we have done the optimization of NW structure for its doping density i.e. what should be the amount of doping density in p-layer and n-layer to get the best possible output in terms of conversion efficiency.

For optimizing the NW structure for its doping, we keep p-layer doping density constant and varying n-layer doping. Figure 6.3 shows the effect of n-layer doping variation on I_{sc} , V_{oc} and conversion efficiency for radial and planar structures. As doping density in n-layer increases recombination centers are increased, which results in

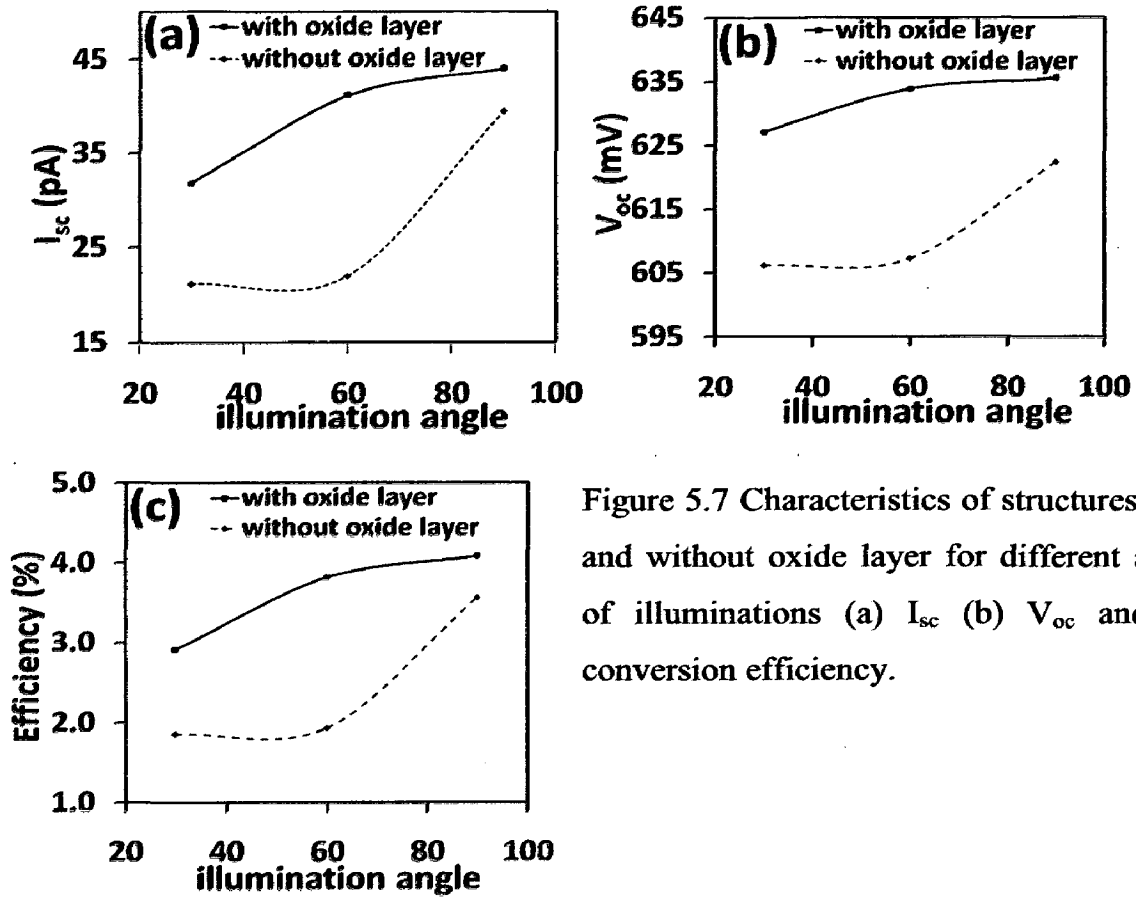


Figure 5.7 Characteristics of structures with and without oxide layer for different angle of illuminations (a) I_{sc} (b) V_{oc} and (c) conversion efficiency.

Our simulation result shows that with increase in incident angle solar cell conversion efficiency increases, with optimum angle of incident comes out to be 90°.

To find the behavior of NW cell at different angle of incident for different wavelength, we have calculated the EQE of NW structure with SiO_2 at different incident angle (Figure 5.8).

We have calculated the EQE using equation (5.3) given as

$$EQE = \frac{Ihc}{q\lambda I_0 S} \quad (5.3)$$

Where h is Plank's constant, c is the speed of light, λ is the wavelength, I_0 is the incident light intensity, I is the photogenerated current and S is the incident surface area.

It is found that with the increase in incident angle, EQE increases for smaller wavelength, while for higher wavelength EQE is almost same for all three different incident angles. This is because as the incident light wavelength increases absorption coefficient decreases due to which EQE decreases with increase in wavelength.

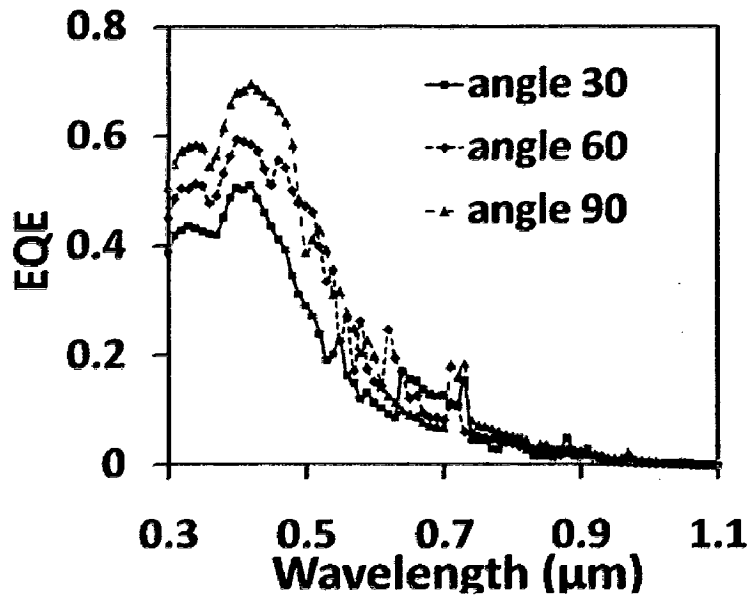


Figure 5.8 EQE for radial structure with SiO₂ layer at different angle of incident.

We get best EQE of value 69.68% at wavelength of 0.42 μm for 90° incident angle. Hence optimization of ARC thickness should be done with keeping in mind that best EQE occurs at wavelength of about 0.42 μm.

5.4 Summary

Using 3D-TCAD simulation we have optimized doping density and i-shell thickness. We find that for a given i-layer thickness, for the best conversion efficiency p and n layer doping density of 10^{18} cm^{-3} and 10^{19} cm^{-3} respectively is needed. The optimized value of i-layer thickness is 80 nm for 380 nm diameter NW structure.

In addition, we studied the effect of defect density present in NW on solar cell performance. It is find that at low defect density of about 10^{12} cm^{-3} radial structure shows 33.50% higher conversion efficiency and while at high defect density of 10^{18} cm^{-3} radial structure shows 118.60% higher conversion efficiency over its planar counterpart. This better performance is attributed to NW cell radial geometry, which gives rise to higher electric field in radial structure than in planar structure.

Illumination angle study shows that optimized angle of solar illumination incident is 90° with the best EQE occurring for a wavelength of 0.42 μm.

Chapter 6

Vertical PN-Nanowire Single and Multijunction Solar Cell

6.1 Vertical PN-Nanowire Solar Cell

6.1.1 Structure Details

The co-axial PN-junction NW structure studied in this work is shown in Figure 6.1 along with its 2D cross section view. In this structure, exterior "shell" of NW is n-type, interior "core" is p-type. Aluminium metal contacts are made on p-core at the bottom and transparent ohmic contact on the top surface of exterior n-shell. A 20 nm thick silicon nitrite (Si_3N_4) layer is used on outer surface for passivation.

For benchmarking purpose, we have created a planar PN-junction structure of same dimensions. Figure 6.2 shows planar structure used for bench marking along with its 2D cross section view.

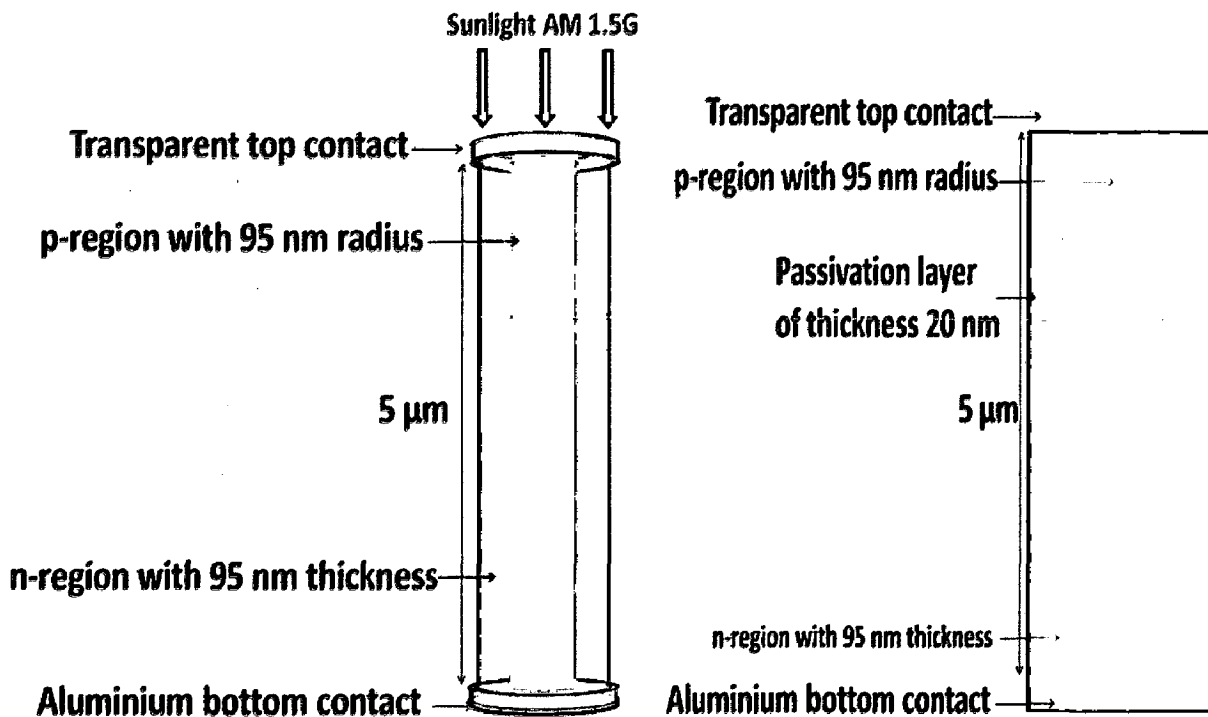


Figure 6.1 On left, 3D view of vertical co-axial PN-junction NW solar cell structure used in this simulation study; on left, 2D cross section view of the same structure.

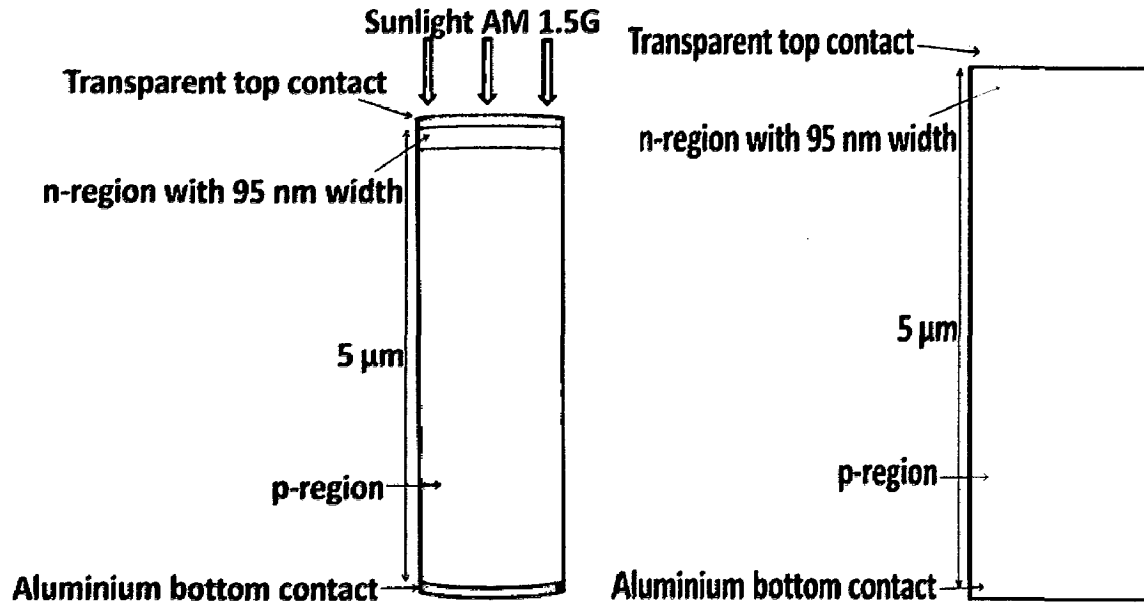


Figure 6.2 On left, 3D view of PN-planar junction solar cell structure used for benchmarking, in this simulation study; on right, 2D cross section view of the same structure.

Table 6.1 shows structural and device model parameters of un-optimized vertical PN-NW cell. Same parameters are also used for planar structure.

Table 6.1 Structure parameters of un-optimized vertical NW solar cell

Parameter	Value	Parameter	Value
Length of NW	5 μm	Si_3N_4 layer thickness	20 nm
p-core radius	95 nm	p-core doping density	10^{16} cm^{-3}
n-shell thickness	95 nm	n-shell doping density	10^{16} cm^{-3}
surface recombination velocity at silicon/ Si_3N_4 interface	10^3 cm^{-2}	surface recombination velocity at silicon/ contact interface	10^5 cm^{-2}
Electron capture cross section	10^{-15} cm^{-2}	Hole capture cross section	10^{-15} cm^{-2}

6.1.2 Structural Parameters Optimization

First of all, we have done the optimization of NW structure for its doping density i.e. what should be the amount of doping density in p-layer and n-layer to get the best possible output in terms of conversion efficiency.

For optimizing the NW structure for its doping, we keep p-layer doping density constant and varying n-layer doping. Figure 6.3 shows the effect of n-layer doping variation on I_{sc} , V_{oc} and conversion efficiency for radial and planar structures. As doping density in n-layer increases recombination centers are increased, which results in

decrease in I_{sc} for planar structure. But for radial structure it increases continuously because of its radial geometry and which give rise to higher electric field.

As doping density of n-layer is increased, built-in potential increases, which in turns increase the V_{oc} . But since NW structure has lager surface area than planar structure, hence there is more surface recombination in NW structure than in planar structure case. This is the reason that radial structure always has V_{oc} smaller than that of planar structure.

From Figure 6.3 (c) the best conversion efficiency for NW structure is obtained with n-layer doping density of 10^{19} cm^{-3} . At this doping density both radial and planar structure both has same conversion efficiency of 4.0%.

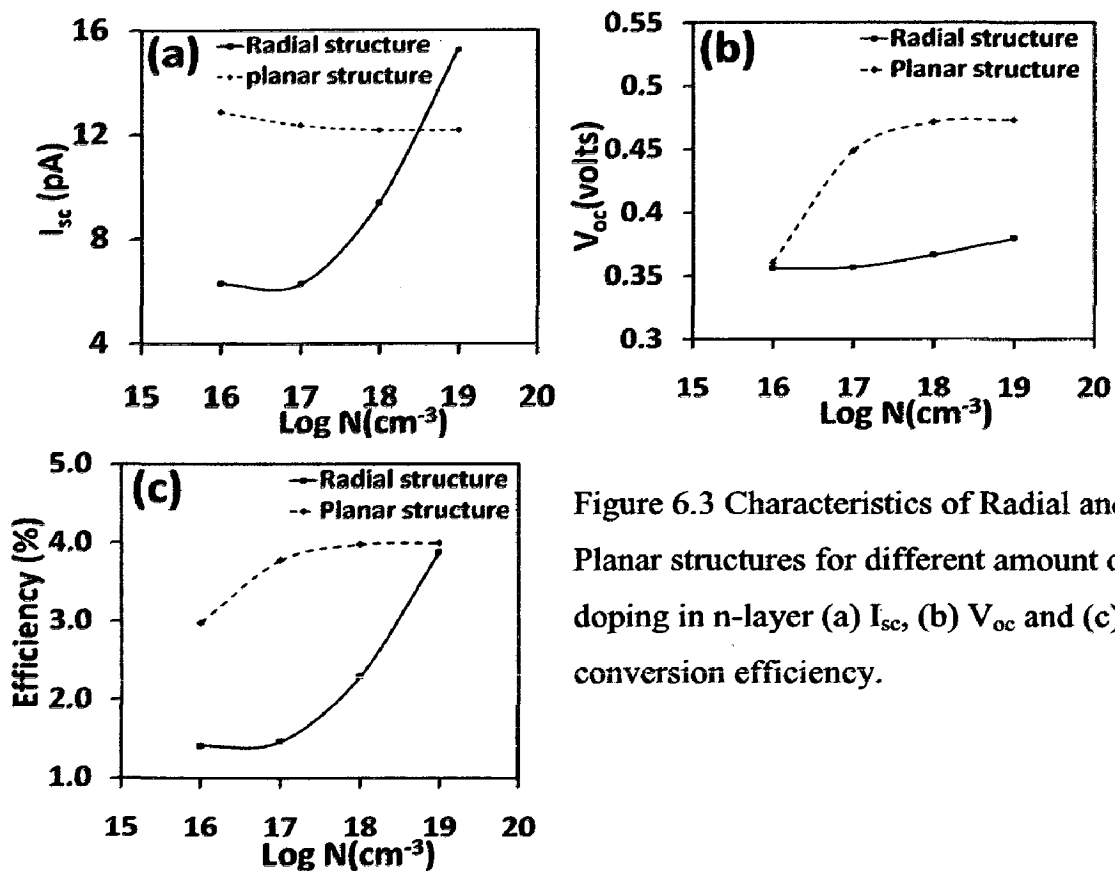


Figure 6.3 Characteristics of Radial and Planar structures for different amount of doping in n-layer (a) I_{sc} , (b) V_{oc} and (c) conversion efficiency.

Figure 6.4 shows the effect of p-layer doping variation on I_{sc} , V_{oc} and conversion efficiency for radial and planar structures. As doping density in p-layer increases I_{sc} of both radial and planar structure reduces.

With increase in doping density in p-layer minority carrier concentration decreases, which in turns decrease the leakage current [17].

6.2 Multijunction Solar Cell

Concept of multijunction is used around the world to enhance the solar cell conversion efficiency. Here we report a novel approach of integrating radial junction and multijunction concept to get enhanced efficiency. We have implemented the GaAs/Si dual junction concept and get efficiency as high as 20%. Although we get this 20% efficiency with un-optimized structure but and are expected to get even higher efficiency with optimized structure [35].

6.2.1 Structure Details

We have created a structure in which top GaAs solar cell is in the form of NW and bottom Si solar cell is planar. Top and bottom solar cell are connected with a hetero tunnel junction. Figure 6.7 shows the multijunction structure studied in this work.

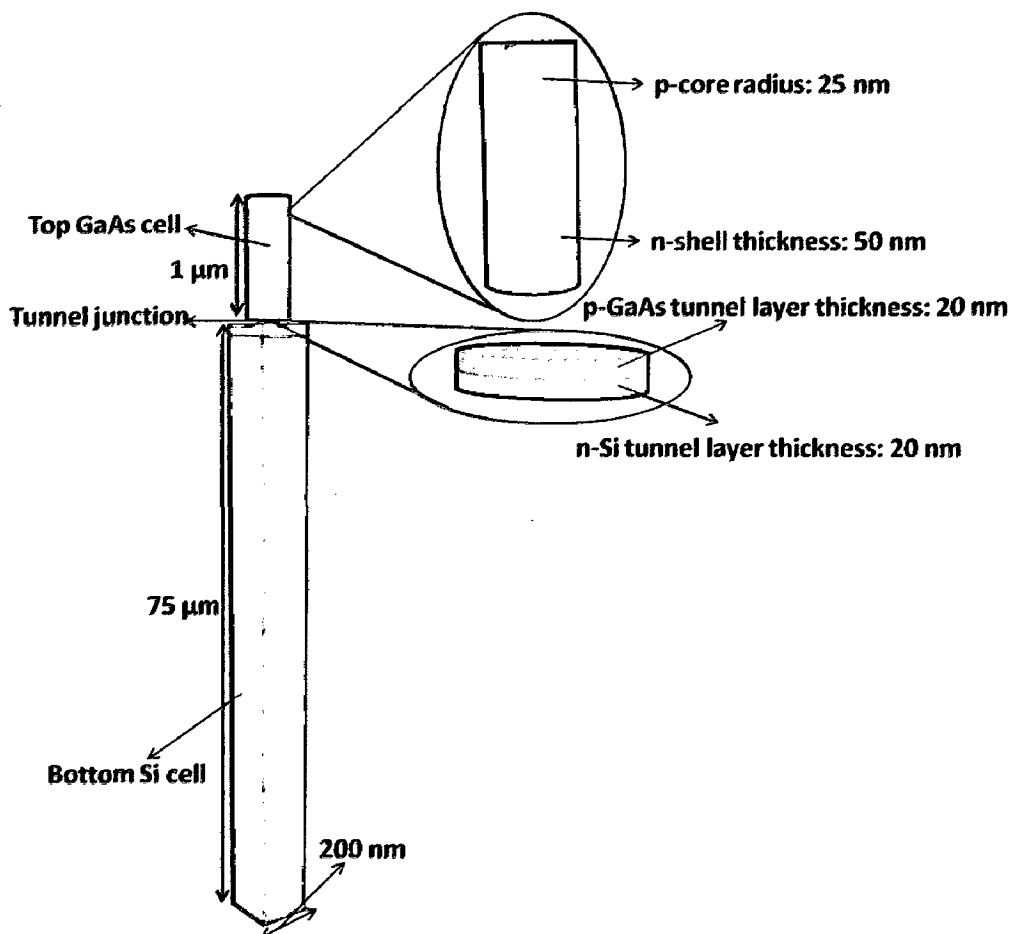


Figure 6.7 Structure of multijunction solar cell.

In this structure, top GaAs NW has exterior "shell" of n-type, interior "core" of p-type. Bottom Silicon cell has top n-type emitter and p-type base. Core of GaAs NW is connected to the emitter of bottom Si-cell through a GaAs/Si tunnel diode. Contacts are made at n-shell top of GaAs-cell and at the base of bottom Si-cell.

Table 6.2 shows structural and device model parameters of un-optimized NW multijunction solar cell.

Table 6.2: Structure parameters of un-optimized NW multijunction solar cell

Parameter	Value	Parameter	Value
Height of GaAs NW	1 μm	p-core radius	25 nm
n-shell thickness	50 nm	p-core doping density	10^{17} cm^{-3}
n-shell doping density	10^{16} cm^{-3}	p-layer tunnel diode thickness	20 nm
n-layer tunnel diode thickness	20 nm	p-layer tunnel doping density	$8 \times 10^{19} \text{ cm}^{-3}$
n-emitter Si-cell doping density	10^{19} cm^{-3}	n-layer tunnel doping density	10^{20} cm^{-3}
Si-cell junction depth	10^{-15} cm^{-2}	p-base Si-cell doping density	10^{16} cm^{-3}
Depth of Si-cell	75 μm	Width/breadth of Si-cell	0.2 μm

6.2.2 Results and Discussion

First of all, we have optimized 1 μm long GaAs NW cell structure, separately, for doping density. p-core radius and n-shell thickness of top GaAs cell used for optimization is 100 nm. The effect of doping density variation in GaAs NW cell is shown in Figures 6.8-6.9.

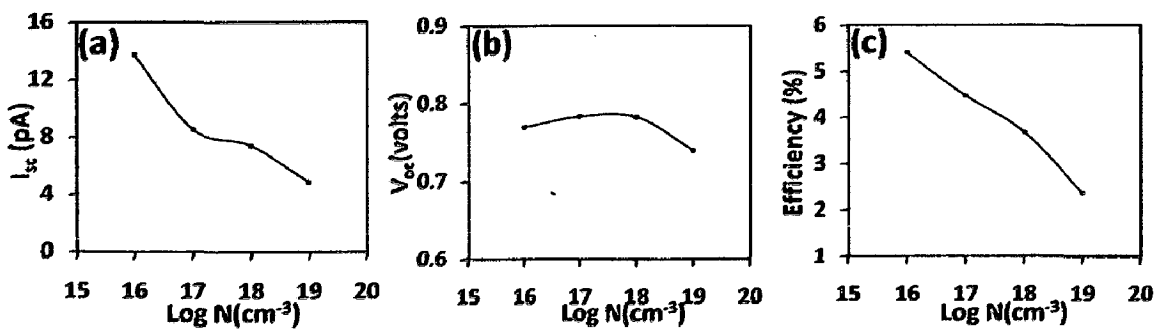


Figure 6.8 Characteristics of GaAs NW cell for different n-shell doping (a) I_{sc} , (b) V_{oc} and (c) conversion efficiency.

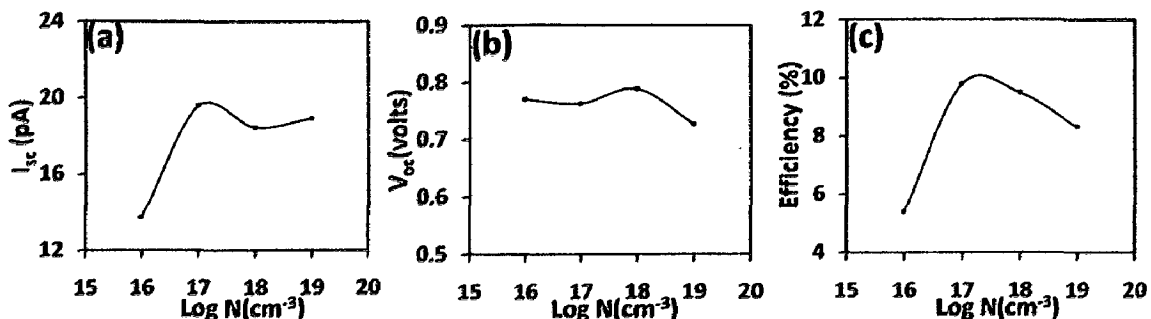


Figure 6.9 Characteristics of GaAs NW cell for different p-core doping (a) I_{sc} , (b) V_{oc} and (c) conversion efficiency.

From above figures optimized value of p-core, n-shell comes out to be 10^{17} cm^{-3} and 10^{16} cm^{-3} respectively.

Although p-core radius and n-shell thickness of top GaAs cell used for optimization is 100 nm, which is different than what we have used in multijunction structure as listed in table III. But since the trend of doping density variation on solar cell performance will remain same and hence optimized value of doping density will remain same irrespective of dimensions.

Top and bottom cell are connected to each other via a GaAs/Si hetero-tunnel diode. We have done the optimization of tunnel diode doping density to get the best peak tunneling current, separately. Figures 6.10 show the band diagrams of tunnel diode for different p and n-layer doping density along with their dimensions and bandgap. Here Figure 6.10 (a)-(b) are for 3D tunnel junction structure and Figure 6.10 (c)-(d) are for 2D tunnel junction structure. As shown by Figure 6.10, we get best tunnel diode for doping density of $8 \times 10^{19} \text{ cm}^{-3}$ and $1 \times 10^{20} \text{ cm}^{-3}$ in p-GaAs and n-Si layers respectively.

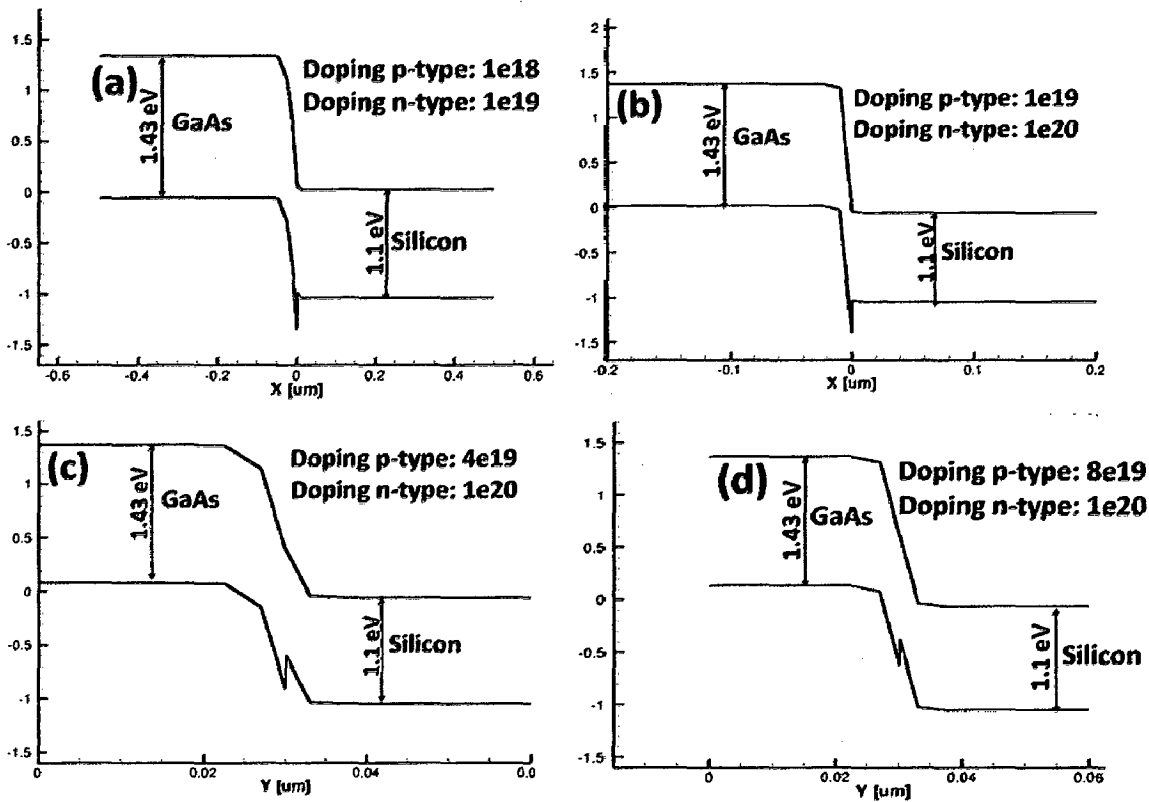


Figure 6.10 Band diagrams of tunnel diode for different doping density.

decrease in I_{sc} for planar structure. But for radial structure it increases continuously because of its radial geometry and which give rise to higher electric field.

As doping density of n-layer is increased, built-in potential increases, which in turns increase the V_{oc} . But since NW structure has larger surface area than planar structure, hence there is more surface recombination in NW structure than in planar structure case. This is the reason that radial structure always has V_{oc} smaller than that of planar structure.

From Figure 6.3 (c) the best conversion efficiency for NW structure is obtained with n-layer doping density of 10^{19} cm^{-3} . At this doping density both radial and planar structure both has same conversion efficiency of 4.0%.

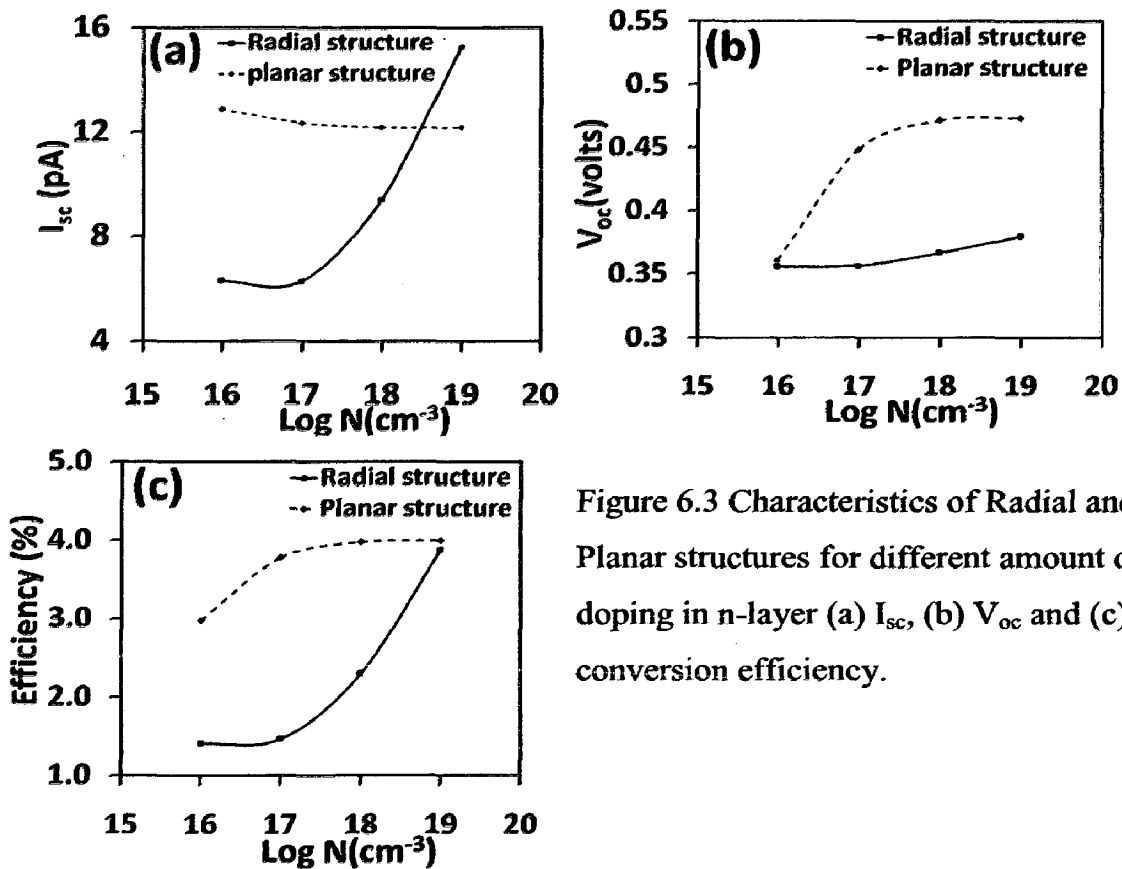


Figure 6.3 Characteristics of Radial and Planar structures for different amount of doping in n-layer (a) I_{sc} , (b) V_{oc} and (c) conversion efficiency.

Figure 6.4 shows the effect of p-layer doping variation on I_{sc} , V_{oc} and conversion efficiency for radial and planar structures. As doping density in p-layer increases I_{sc} of both radial and planar structure reduces.

With increase in doping density in p-layer minority carrier concentration decreases, which in turns decrease the leakage current [17].

$$I_o = \frac{qAD_p p_{no}}{L_p} + \frac{qAD_n n_{po}}{L_n} \quad (6.1)$$

This reduction in leakage current will increase V_{oc} as indicated by equation (1.6). From simulation results the optimized value of p-core and n-shell doping density are 10^{19} cm^{-3} and 10^{19} cm^{-3} respectively.

Although V_{oc} of NW structure is low as compare to planar structure, but since NW structure has higher I_{sc} than planar structure as a result overall conversion efficiency of NW structure is 1.36 times higher than that of planar structure.

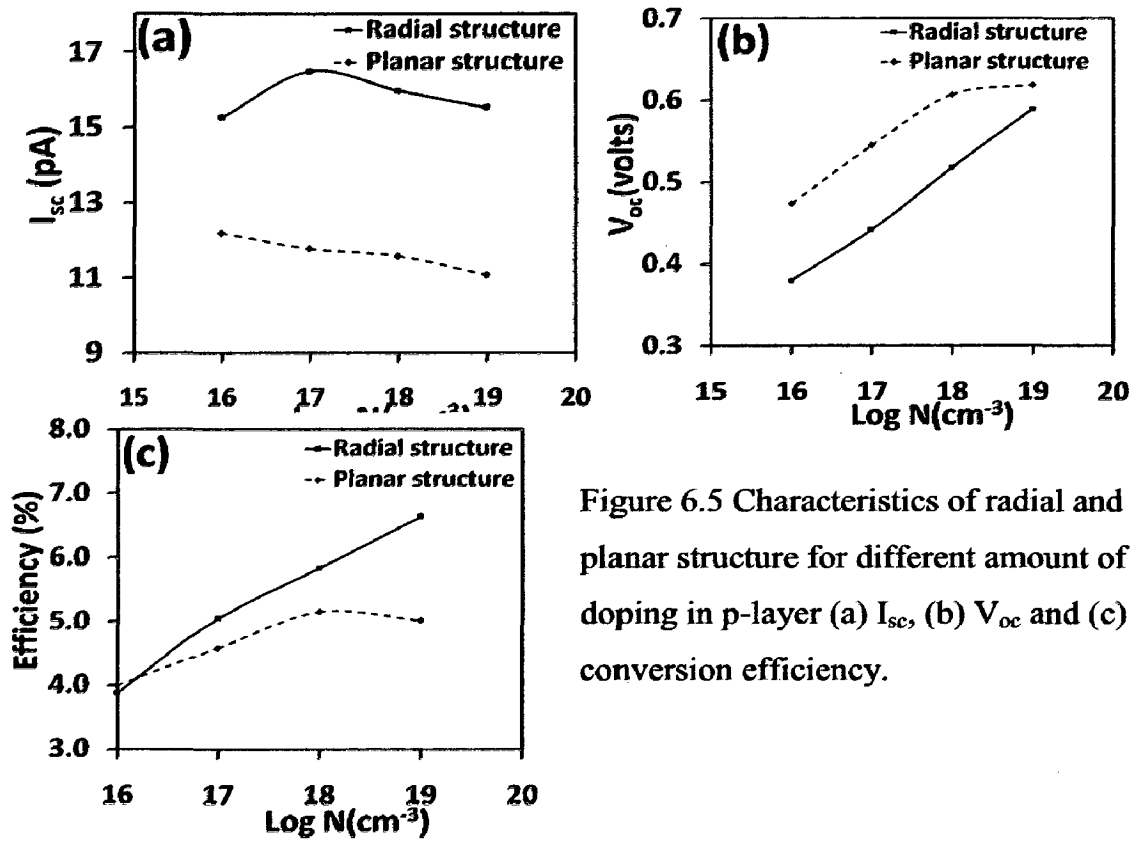


Figure 6.5 Characteristics of radial and planar structure for different amount of doping in p-layer (a) I_{sc} , (b) V_{oc} and (c) conversion efficiency.

To compare the performance of radial and planar structures with different amount of defect density present in it, we have intentionally introduced donor type defects at intrinsic energy level in silicon of both radial and planar structures.

Figure 6.6 shows the effect of defect density on I_{sc} , V_{oc} and conversion efficiency for radial and planar structures. As trap density increases minority carrier life time and hence diffusion length decreases. Since NW structure has junction in radial direction, this reduction in diffusion length does not affect radial junction solar cell performance as a

results I_{sc} remains constant even with high as high as 10^{18} cm^{-3} amount of defect density. While for the case of planar case it gets reduced.

Since increasing trap density increase recombination centers, which in turns increases recombination current resulting decrease in V_{oc} as shown by Figure 6.6 (b).

At low defect density of about 10^{12} cm^{-3} radial structure shows 24.62% better conversion efficiency and at high defect density as high as 10^{18} cm^{-3} radial structure shows 82.36% better conversion efficiency over its planar counterpart.

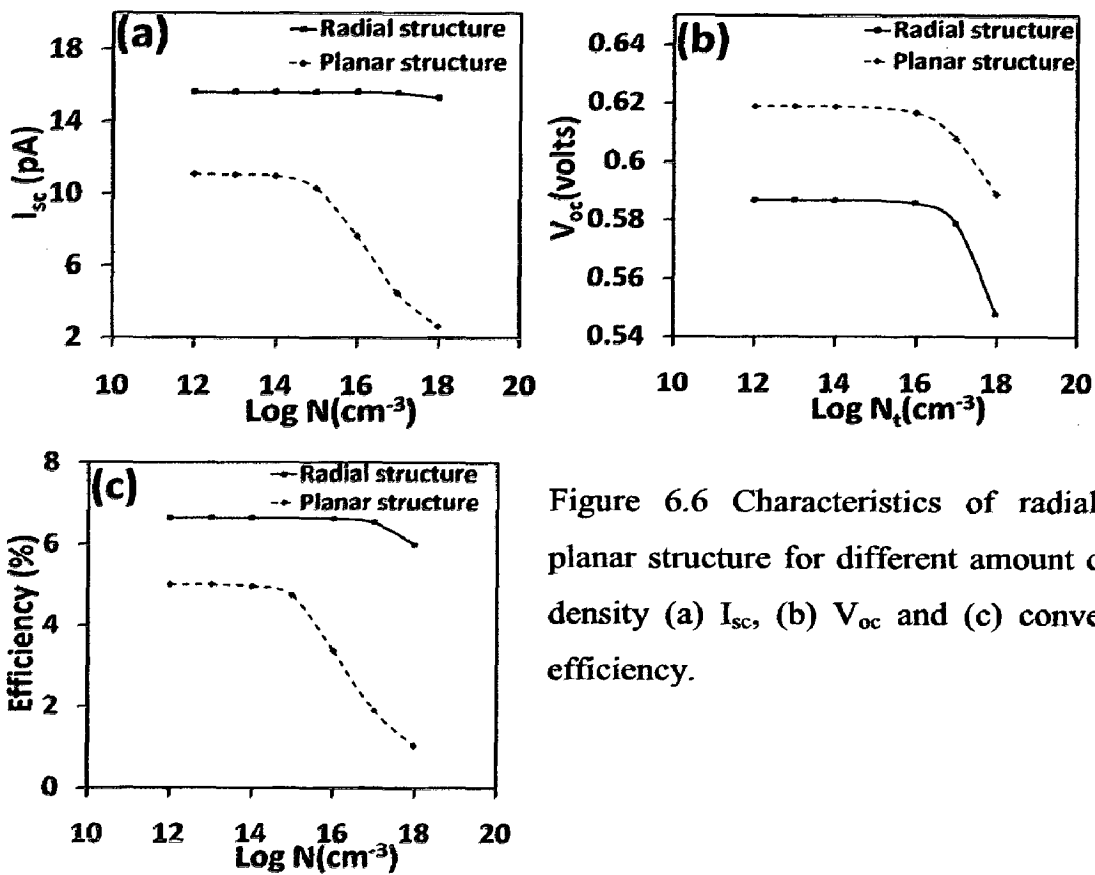


Figure 6.6 Characteristics of radial and planar structure for different amount defect density (a) I_{sc} , (b) V_{oc} and (c) conversion efficiency.

6.1.3 Summary

Using 3D-TCAD simulation, we have optimized doping density. We find that the best output in terms of conversion efficiency occurs for p and n layer doping density of 10^{19} cm^{-3} . In addition, we studied the effect of defect density present in NW on solar cell performance. It is found that even with high defect density, as high as 10^{18} cm^{-3} , radial structure has 82.36% higher conversion efficiency over its planar counterpart.

6.2 Multijunction Solar Cell

Concept of multijunction is used around the world to enhance the solar cell conversion efficiency. Here we report a novel approach of integrating radial junction and multijunction concept to get enhanced efficiency. We have implemented the GaAs/Si dual junction concept and get efficiency as high as 20%. Although we get this 20% efficiency with un-optimized structure but and are expected to get even higher efficiency with optimized structure [35].

6.2.1 Structure Details

We have created a structure in which top GaAs solar cell is in the form of NW and bottom Si solar cell is planar. Top and bottom solar cell are connected with a hetero tunnel junction. Figure 6.7 shows the multijunction structure studied in this work.

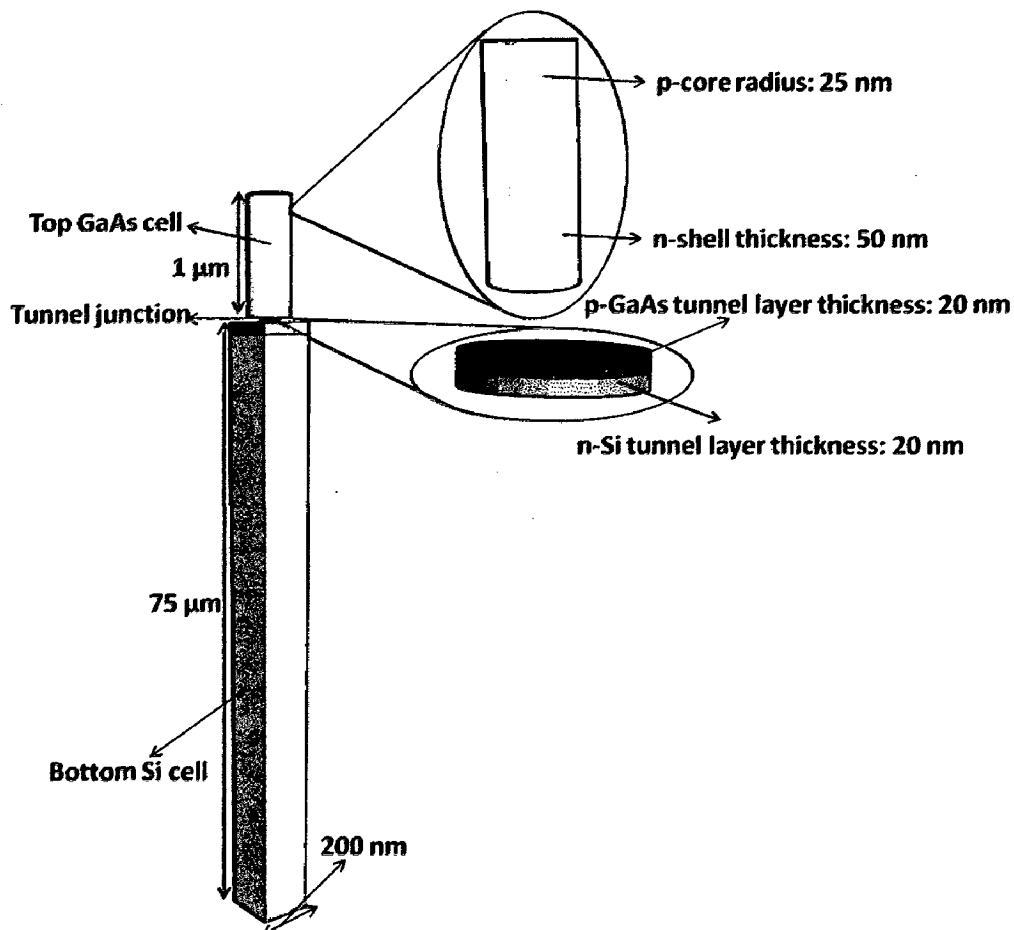


Figure 6.7 Structure of multijunction solar cell.

In this structure, top GaAs NW has exterior "shell" of n-type, interior "core" of p-type. Bottom Silicon cell has top n-type emitter and p-type base. Core of GaAs NW is connected to the emitter of bottom Si-cell through a GaAs/Si tunnel diode. Contacts are made at n-shell top of GaAs-cell and at the base of bottom Si-cell.

Table 6.2 shows structural and device model parameters of un-optimized NW multijunction solar cell.

Table 6.2: Structure parameters of un-optimized NW multijunction solar cell

Parameter	Value	Parameter	Value
Height of GaAs NW	1 μm	p-core radius	25 nm
n-shell thickness	50 nm	p-core doping density	10^{17} cm^{-3}
n-shell doping density	10^{16} cm^{-3}	p-layer tunnel diode thickness	20 nm
n-layer tunnel diode thickness	20 nm	p-layer tunnel doping density	$8 \times 10^{19} \text{ cm}^{-3}$
n-emitter Si-cell doping density	10^{19} cm^{-3}	n-layer tunnel doping density	10^{20} cm^{-3}
Si-cell junction depth	10^{-15} cm^{-2}	p-base Si-cell doping density	10^{16} cm^{-3}
Depth of Si-cell	75 μm	Width/breadth of Si-cell	0.2 μm

6.2.2 Results and Discussion

First of all, we have optimized 1 μm long GaAs NW cell structure, separately, for doping density. p-core radius and n-shell thickness of top GaAs cell used for optimization is 100 nm. The effect of doping density variation in GaAs NW cell is shown in Figures 6.8-6.9.

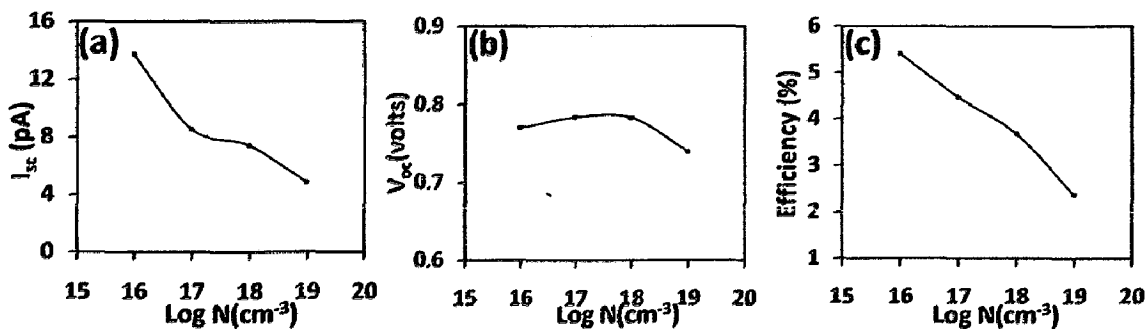


Figure 6.8 Characteristics of GaAs NW cell for different n-shell doping (a) I_{sc} , (b) V_{oc} and (c) conversion efficiency.

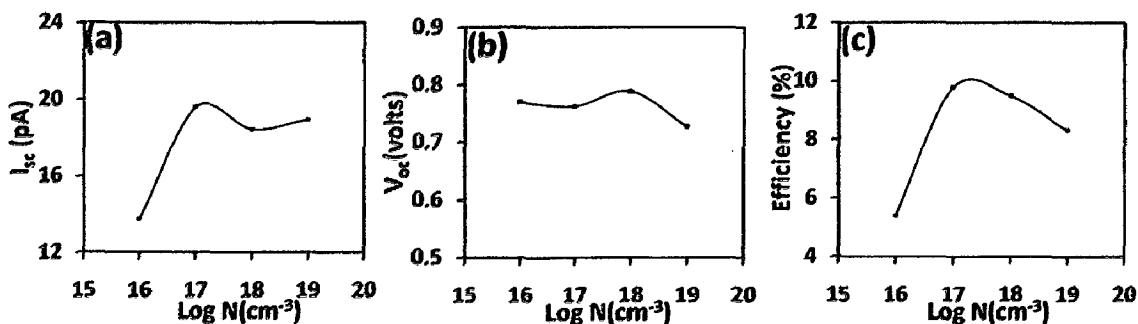


Figure 6.9 Characteristics of GaAs NW cell for different p-core doping (a) I_{sc} , (b) V_{oc} and (c) conversion efficiency.

From above figures optimized value of p-core, n-shell comes out to be 10^{17} cm^{-3} and 10^{16} cm^{-3} respectively.

Although p-core radius and n-shell thickness of top GaAs cell used for optimization is 100 nm, which is different than what we have used in multijunction structure as listed in table III. But since the trend of doping density variation on solar cell performance will remain same and hence optimized value of doping density will remain same irrespective of dimensions.

Top and bottom cell are connected to each other via a GaAs/Si hetero-tunnel diode. We have done the optimization of tunnel diode doping density to get the best peak tunneling current, separately. Figures 6.10 show the band diagrams of tunnel diode for different p and n-layer doping density along with their dimensions and bandgap. Here Figure 6.10 (a)-(b) are for 3D tunnel junction structure and Figure 6.10 (c)-(d) are for 2D tunnel junction structure. As shown by Figure 6.10, we get best tunnel diode for doping density of $8 \times 10^{19} \text{ cm}^{-3}$ and $1 \times 10^{20} \text{ cm}^{-3}$ in p-GaAs and n-Si layers respectively.

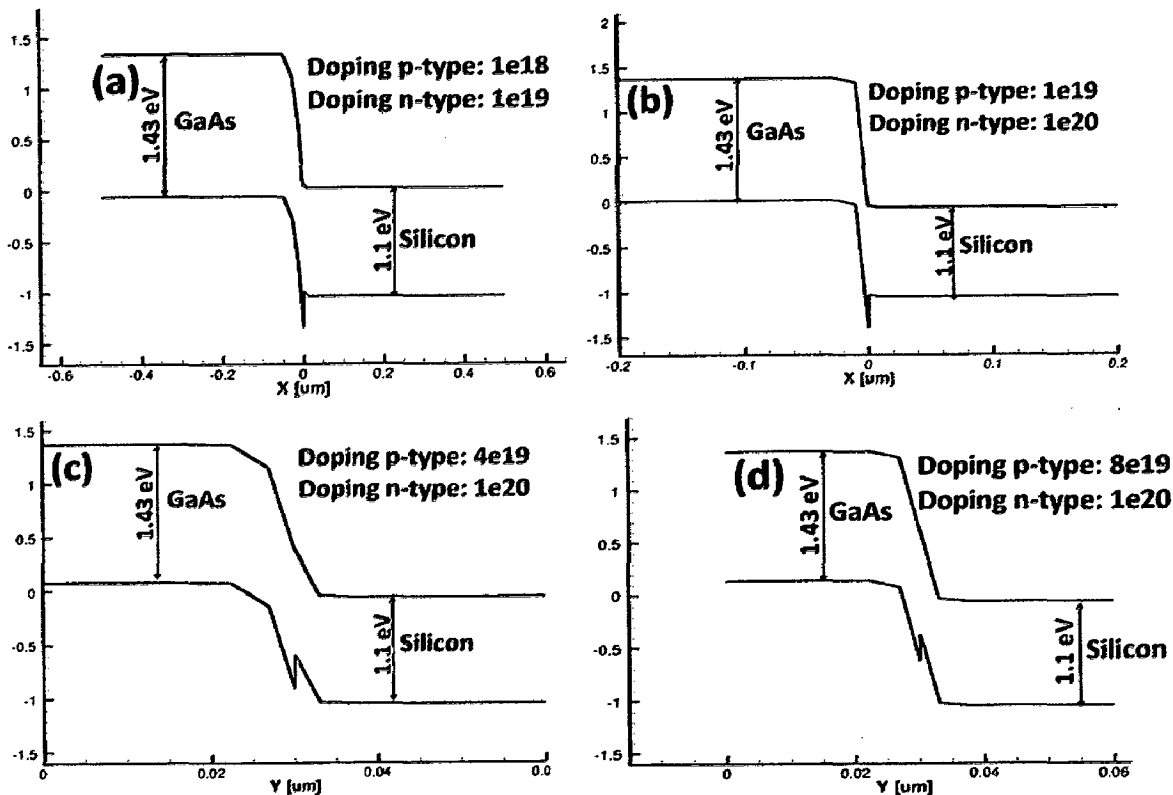


Figure 6.10 Band diagrams of tunnel diode for different doping density.

Total power incident on multijunction solar cell is calculated by multiplying power density of A.M. 1.5G solar spectrum (0.1 W/cm^2) with top cross section of Si-cell. With this un-optimized structure we obtain an I_{sc} of 2.65 pA and V_{oc} of 0.967 giving conversion efficiency of 20.57%.

6.2.3 Summary

In this study, we have implemented the GaAs/Si dual junction concept and obtain conversion efficiency as high as 20% with un-optimized structure. We are expected to achieve even higher efficiency with the optimized structure. There are following parameters, which are needed to be optimized.

1. p-core radius of top cell.
2. Height of top and bottom cell to match the I_{sc} of the both cells.
3. ARC, although we have not used ARC in this study.

Chapter 7

Conclusion and Future Work

In this thesis we have explored the ability of radial junctions to enable PV device to have high conversion efficiency despite using low grade material. Using 3D-TCAD simulation we have optimized doping density, i-shell thickness. We have modeled and studied the effect of electric field on cell performance in radial junction structures. It is seen that the performance of cell is strongly enhanced by increased electric field. In addition we studied the effect of defect density present in cell on its performance.

We have modeled and simulated the electric field inside PIN and PN junction NW structure with very good matching is obtained in i-layer of PIN structure. We note that peak electric field at p/i interface in PIN-NW structure is 1.53 times higher than the peak electric field in planar structure for the doping density of 10^{18} cm^{-3} and 10^{19} cm^{-3} in p-core and n-shell respectively. Similarly for PN-NW structure results show that for a doping density of 10^{19} cm^{-3} in p-core and n-shell, peak electric field in PN-NW structure at p/n-interface is 1.33 times higher than that at p/n-interface in planar structure. This is the main reason of radial structure having higher conversion efficiency compared to planar structure.

Using 3D-TCAD simulation, we have optimized doping density and i-shell thickness of lateral PIN-NW structure. We find that for a given i-layer thickness, the best conversion efficiency occurs for p and n layer doping density of 10^{18} cm^{-3} and 10^{19} cm^{-3} respectively. The optimized value of i-layer thickness is found to be 80 nm for 380 nm diameter NW structure.

In addition, we studied the effect of defect density present in PIN-NW solar cell structure on its performance. It is found that at low defect density of about 10^{12} cm^{-3} radial structure shows 33.50% higher conversion efficiency while at high defect density of 10^{18} cm^{-3} radial structure shows 118.60% higher conversion efficiency over its planar

counterpart. This better performance is attributed to NW cell radial geometry, which gives rise to higher electric field than in planar structure.

Illumination angle study shows that optimized angle of solar illumination incident is 90° with the best EQE occurring at a wavelength of $0.42 \mu\text{m}$. Hence, optimization of ARC thickness should be done keeping in mind that best EQE occurs at wavelength of about $0.42 \mu\text{m}$. This study serves as future guideline for designing and developing NW solar cell and application devices.

We have also optimized the doping density in vertical PN-NW structure. We find that the best output in terms of conversion efficiency occurs for p and n layer doping density of 10^{19}cm^{-3} . In addition, we studied the effect of defect density present in NW on solar cell performance. It is found that even with high defect density, as high as 10^{18}cm^{-3} , radial structure has 82.36% higher conversion efficiency over its planar counterpart.

We have introduced a novel way of using multijunction concept in NW solar cell. We have implemented GaAs/Si Heterojunction in making multijunction solar cell and obtain a conversion efficiency of 20% for un-optimized structure.

Future study should address the need of optimization of ARC coating thickness and light trapping effect to achieve enhanced conversion efficiency. Considerable effort is needed to optimize radial multijunction structure. We need to do current matching of top and bottom cell, optimize the top cell NW diameter and ARC coating.

Bibliography

1. Bin Li, L. Wang, B. Kang, P. Wang and Y. Qiu, "Review of recent progress in solid-state dye-sensitized solar cells", *Solar Energy Materials & Solar Cells*, Vol. 90, pp. 549-573, 2006.
2. E. S. Aydil, "Nanomaterials for solar cells", *Nanotechnology law & Business*, Vol. 4, Issue 3, pp. 275-291, 2007.
3. W. Shockley and H. J. Queisser, "Detail balance limit of efficiency of p-n junction solar cells", *Journal of Applied Physics*, Vol. 32, pp. 510-519, 1961.
4. G. B. Haxel, J. B. Hedrick, and G. J. Orris, "Rare earth elements-critical resources for high technology", *US Geological Survey fact sheet 087-02*. Technical report, US Geological Survey, 2002.
5. A. Luque and S. Hegedus, "Handbook of Photovoltaic Science and Engineering", John Wiley & Sons, 2003.
6. C. J. Brabec, N. S. Sariciftci and J. C. Hummelen, "Plastic solar cells", *Journal of Advanced Functional Materials*, Vol. 11, Issue 1, pp. 15-26, 2001.
7. L. M. Chen, Z. Hong, G. Li and Y. Yang, "Recent progress in polymer solar cells: Manipulation of polymer: fullerene morphology and the formation of efficient inverted polymer solar cells", *Journal of Advanced Functional Materials*, Vol. 21, pp. 1434-1449, 2009.
8. M. Law, L. E. Greene, J. C. Johnson, R. Saykally and P. Yang Lewis, "Nanowire Dye-Sensitized Solar cells", *Nano Letters*, Vol. 4, pp. 455-459, 2005.
9. B. Tian, X. Zheng, T. J. Kempa, Y. Fang, N. Yu, G. Yu, J. Huang and C. M. Lieber, "Coaxial silicon nanowires as solar cells and nanoelectronic power sources", *Nature Letters*, Vol. 449, pp. 885-890, 2007.
10. B. M. Kayes, H. A. Atwater and N. S. Lewis, "Comparison of device physics principles of planar and radial p-n junction nanorods solar cells", *Journal of Applied Physics*, Vol. 97, pp. 114302-1-114302-11, 2005.
11. O. Gunawan, S. Guha, "Characteristics of vapor-liquid-solid grown silicon nanowire solar cells", *Solar Energy Materials & Solar Cells*, Vol. 93, pp. 1388-1393, 2009.

12. C. Y. Kuo, C. Gau, B. T. Dai, "Photovoltaic characteristics of silicon nanowire arrays synthesized by vapor–liquid–solid process", *Solar Energy Material & Solar Cells*, Vol. 95, pp. 154-157, 2010.
13. W. F. Liu, J. I. Oh, and W. Z. Shen, "Light trapping in single coaxial nanowires for photovoltaic applications", *IEEE Electron Device Letters*, Vol. 32, Issue 1, pp. 45-47, 2011.
14. V. Sivakov, G. Andrä, A. Gawlik, A. Berger, J. Plentz, F. Falk, and S.H. Christiansen, "Silicon nanowire based solar cells on glass: synthesis, optical properties, and Cell parameters", *Nano Letters*, Vol. 9, Issue 4, pp. 1549-1554, 2009.
15. L. Tsakalakos, J. Balch, J. Fronheiser, B. A. Korevaar, O. Sulima and J. Rand, "Silicon nanowire solar cells", *Applied Physics Letters*, Vol. 91, pp. 233117-1-233117-3, 2007.
16. E. Garnett and P. Yang, "Light trapping in silicon nanowire solar cells", *Nano Letters*, Vol. 10, pp. 1082-1087, 2010.
17. S. M. Sze, "Physics of Semiconductor Devices", Wiley, New York, 2nd edition, 1981.
18. T. Markvart and L. Castaner, "Solar Cells Materials Manufacture and Operation", Elsevier publication, 2005.
19. National Department of Energy, <http://rredc.nrel.gov/solar/spectra>, "U.S. Department of Energy", Description of Air Mass.
20. M. J. Archer, "Multijunction Solar Cells on Epitaxial Templates", Ph.D. Thesis, California Institute of Technology Pasadena, California, 2005.
21. M. D. Katzenberg, D. B. Turner, B. M. Kayes, M. A. Filler, M. C. Putnam, N. S. Lewis and H. A. Atwater, "Single nanowire Si solar cells", *Nano Letter*, Vol. 8, Issue 2, pp. 710-714, 2008.
22. Wei Lu and Charles M Lieber, "Topical review of semiconductor nanowires", *Journal of Applied Physics*, Vol. 39, pp. R387–R406, 2006.
23. M. Tang, Shu-Tong Chang, Tzu-Chun Chen, Z. Pei, Wei-Ching Wang, J. Huang, "Simulation of nanorod structures for an amorphous silicon-based solar cell", *Thin Solid Films*, Vol. 518, pp. S259–S261, 2010.
24. Michael Grätzel, "Review dye-sensitized solar Cells", *Journal of Photochemistry and Photobiology*, Vol. 4, pp. 145–153, 2003.
25. H. J. Prall, "Tandem Solar Cells", Ph.D. Thesis, Linz Institute for Organic Solar Cells (LIOS), Germany, 2005.

26. V. Consonni, G. Rey, J. Bonaime, N. Karst, B. Doisneau, H. Roussel, S. Renet and D. Bellet, "Synthesis and physical properties of ZnO/CdTe core shell nanowires grown by low-cost deposition methods", *Applied Physics Letters*, Vol. 91, 233117, 2007.
27. R. Kapadia, Z. Fan and A. Javey, "Design constraints and guidelines for CdS/CdTe nanopillars based photovoltaic", *Applied Physics Letters*, Vol. 96, 103116-1-103116-3, 2010.
28. Y. B. Tang, Z. H. Chen, H. S. Song, C. S. Lee, H. T. Cong, H. M. Cheng, W. J. Zhang, I. Bello, and S. T. Lee, "Vertically aligned p-type single-crystalline GaN nanorod arrays on n-type Si for heterojunction photovoltaic Cells", *Nano Letters*, Vol.8, Issue 12, pp. 4191-4195, 2008.
29. P. C. Dhanasekaran, B. S. V. Gopalam, "Influence of minority carrier diffusion length in determining the effects of base layer thickness of an n+p silicon cell and a BSF cell by numerical analysis", *Journal of Material Science Letters*, Vol. 6, pp. 1156-1160, 1987.
30. H. Cotal, C. Fetzer, J. Boisvert, G. Kinsey, R. King, P. Hebert, H. Yoon and N. Karam, "III-V multijunction solar cells for concentrating photovoltaics", *Energy & Environmental science*, Vol. 2, pp. 174-192, 2009.
31. B. M. Kayes, "Radial pn Junction, Wire Array Solar Cells", Ph.D. Thesis, California Institute of Technology Pasadena, California, 2009.
32. Synopsys, "Sentaurus TCAD user manual", 2010.
33. B. J. Baliga, "Modern Power Devices", John Wiley & Sons, 1987.
34. B. V. Zeghbroeck, "Principle of Semiconductor Devices", Chapter 4, University of Colorado, 2007.
35. J. M. Gee, G. F. Virshup, "A 31% efficient GaAs/Silicon mechanically stacked, multijunction concentrator solar cell", *IEEE Photovoltaic Specialists Conference*, Vol. 1, pp. 754-758, 1988.

List of Publications

1. *Jitendra kumar*, S. K. Manhas, Dharmendra Singh, A. K. Saxena and B. K. Kaushik (2011), "Optimization of lateral Silicon Nanowire based Solar cell using 3D-TCAD Simulation", *15th-VLSI Design AND Test Symposium-2011, Pune, June 7-9, 2011, (Accepted)*.
2. *Jitendra kumar*, S. K. Manhas, Dharmendra Singh, "Optimization of Vertical Silicon Nanowire based Solar cell using 3D TCAD Simulation", *13th-International Symposium on Integrated Circuits, Singapore, December 12-14, 2011, (Communicated)*.